Journal of Vibration Engineering & Technologies (2026) 14:102
https://doi.org/10.1007/s42417-025-02273-y

ORIGINAL PAPER

# A Vibration-Driven Computational Method for Localizing Interfacial Debonding in Concrete-Filled Steel Tubes

**Alireza Safari Tarbozagh[1] · Mohtasham Khanahmadi[2] · Denise-Penelope N. Kontoni[3,4] · Behzad Dezhkam[5] · Saman Mansouri[6]**

Received: 15 July 2025 / Revised: 16 October 2025 / Accepted: 7 December 2025


## Abstract

**Background** Concrete-Filled Steel Tube (CFST) composite columns are widely utilized in civil engineering structures due to their high structural efficiency and superior load-bearing capacity. However, interfacial debonding between the steel tube and the concrete core constitutes a critical damage mechanism that can significantly alter the dynamic response and compromise structural integrity.

**Purpose** This study proposes a novel vibration-driven computational methodology for detecting and localizing interfacial debonding in CFST columns.

**Methods** The proposed methodology employs curvature analysis of the initial (intact) and current vibration mode shapes and introduces the Irregularity Detection Index (IDI) as a robust damage indicator. Vibration mode shapes are obtained through finite element analysis and are subsequently post-processed within a numerical computing platform to evaluate the IDI and identify damage locations.

**Results** Numerical results demonstrate that the proposed algorithm accurately detects interfacial debonding between the concrete core and the steel tube. The method exhibits high sensitivity in detecting damage near boundary edges and at the column base, regions that are typically challenging for structural health monitoring (SHM). Furthermore, reliable diagnostic performance is maintained under low-level simulated noise, confirming the robustness of the approach.

**Conclusions** The proposed vibration-based computational methodology provides an accurate and robust tool for detecting and localizing interfacial debonding in CFST composite columns. Its effectiveness in identifying damage in boundary regions and at the column base, together with its stability under low-level noise conditions, highlights its strong potential for practical SHM applications.

**Keywords** Concrete-Filled Steel Tube (CFST) · Vibration mode shapes · Interfacial debonding detection · Irregularity detection index (IDI) · Structural health monitoring (SHM)

✉ Denise-Penelope N. Kontoni
kontoni@uop.gr; kontoni.denise@ac.eap.gr

Alireza Safari Tarbozagh
safari_a@rail.iust.ac.ir

Mohtasham Khanahmadi
mohtashamkhanahmadi@semnan.ac.ir

Behzad Dezhkam
b.dezhkam@velayat.ac.ir

Saman Mansouri
s.mansouri@phd.unistrapg.it

[1] School of Railway Engineering, Iran University of Science and Technology, Tehran, Iran

[2] Faculty of Civil Engineering, Semnan University, Semnan, Iran

[3] Department of Civil Engineering, School of Engineering, University of the Peloponnese, Patras GR-26334, Greece

[4] School of Science and Technology, Hellenic Open University, Patras GR-26335, Greece

[5] Department of Civil Engineering, Velayat University, Iranshahr, Iran

[6] Water Resources Research and Documentation Center (WARREDOC), Università per Stranieri di Perugia, Perugia, Italy

Published online: 17 February 2026

## Introduction

Structural health monitoring (SHM) and the detection of potential damages are fundamental aspects in civil engineering and structural safety. Early detection of damages can prevent serious issues and costly repairs, ensuring structural longevity. Among various approaches, dynamic response-based methods have gained interest for identifying subtle damage. Analyzing deformation patterns, natural frequencies, and dynamic parameters are effective strategies for SHM. Non-destructive diagnostic methods, such as wavelet-based signal processing among others, as well as advanced repair techniques using self-compacting concrete and functionally graded plates [1, 2], have been successfully applied to detect defects in structural elements, demonstrating the potential of advanced monitoring techniques for structural evaluation [3–7]. Recent comprehensive review studies on vibration-based SHM systems and structural vibration control have further emphasized the integration of modern sensing technologies and energy dissipation devices — such as lead rubber bearings, elastomeric bearings, and friction pendulum bearings — to enhance structural resilience and reduce damage under dynamic loading [8–11]. These studies provide comprehensive reviews and examples of advanced sensor technologies, signal processing techniques, and computational frameworks, demonstrating how modern SHM systems can reliably detect, localize, and evaluate structural damage. In this context, various studies have explored methods for detecting structural damage, significantly improving diagnostic techniques and strengthening SHM reliability.

Pandey et al. [12] utilized mode shape curvature analysis to locate damage in cantilever and simply supported beams, highlighting its responsiveness to applied defects. In another study, Yam et al. [13] introduced a damage assessment index derived from mode shape curvature and examined its capability in detecting crack defects in an aluminum thin plate. Sahoo et al. [14] employed a neural genetic algorithm to assess the health of a structure, implementing it based on the significant impact of damage on the static behavior of the structure. Shih et al. [15] investigated the modal strain energy index for damage detection, showing its ability to identify damage in girders and bridge decks. Roveri and Carcaterra [16] implemented empirical mode decomposition (EMD) to monitor damage in bridges exposed to transient loads, accurately identifying the damage by extracting peak pulses in the first vibration mode. Bao et al. [17] proposed a multi-level diagnostic technique grounded in EMD, which efficiently identified damage by computing momentary frequencies from vibration responses. Xu et al. [18] suggested a method based on smooth curvature, accounting for the impact of adjacent element length differences, demonstrating its capability to detect damage. In another study, Sun and Ren [19] applied wavelet transform (WT) for seismic damage analysis in a gravity concrete dam, proposing a global damage index that simulated the overall damage degree of the dam under seismic activities. Nobahari et al. [20] proposed a search-based algorithm for identifying damage locations with sound echo, utilizing a cost function that included natural frequency changes. Abbasnia et al. [21] developed a dual-phase strategy to identify and measure structural damage in beams, utilizing WT and the improved colliding bodies optimization (ECBO) technique for correcting the estimation of errors. Mirzaei et al. [22] applied a similar approach for long trusses, utilizing WT and static deflection for damage localization and the artificial bee colony (ABC) method used in model calibration, thereby enhancing accuracy and reducing computational effort. Yang et al. [23] used a simple method based on the Fourier spectrum to calculate mode shape curvature, applying this information for damage detection in beams. Yang and Oyadiji [24] employed a modal frequency surface (MSF) for damage identification in multi-layered composite plates, indicating that a reduction in the local stiffness of layers disturbs the MSF, and using wavelet coefficients of this surface allowed for determining the location and shape of damage. Kourehli [25] proposed an efficient damage detection method for plate structures using extreme learning machine (ELM), applying mode shapes and natural frequencies as inputs for identifying damage states in plate elements. Darvishan [26] proposed a frequency-domain analysis and clustering-based approach for detecting damage in cable-stayed bridges, introducing a damage index using Euclidean distance between cluster centers, which effectively discriminated between healthy and damaged states. Hanteh et al. [27, 28] applied continuous WT (CWT) and mode shape analysis for damage identification in a fully panelized building structure, identifying damage locations through maximum and minimum relative jumps in wavelet coefficients. Bakhshi and Mousavi [29, 30] used deep learning for crack detection in masonry and concrete structures, demonstrating that their proposed method outperforms other image processing methods in terms of accuracy. Ghannadi and Kourehli [31] utilized the slime mold algorithm (SMA) and marine predators algorithm (MPA) for damage detection in large-scale structures, comparing them with other optimization techniques, and showing that SMA combined with the modified total modal assurance criterion (MTMAC) provided accurate damage identification, with the improved SMA (ISMA) offering significant benefits in global optimization and finite element model updating. Silik et al. [32] proposed a novel technique for extracting features sensitive to damage and constructing a statistical approach utilizing pattern identification. The identified features were embedded into an

AI-driven network designed for classifying structural damage, leveraging wavelet energy. The method demonstrated its efficacy in assessing the integrity of large, complex structures through experimental data obtained from a multi-story building structure, proving reliable even under noisy conditions and random dynamic excitations. Chen et al. [33] suggested a damage identification approach for bridges by combining Quasi-static displacement-induced linearity error curves (QSDIL) and wavelet packet decomposition (WPD). By integrating these two damage indicators, the method effectively localized and accurately identified structural damage under diverse conditions, including noise interference and variable vehicle weights, with robust experimental validation. Kordestani et al. [34] proposed an energy-driven, output-only approach for detecting structural damage, leveraging trendlines derived from structural acceleration responses. By applying a Savitzky–Golay filter to process and break down these trendlines, their method effectively pinpointed and quantified structural damage, even under noisy conditions, without relying on modal properties. The approach exhibited high precision across computational analyses and real-world experimental validations. Zhou et al. [35] developed an approach to detecting structural deterioration in steel girders by analyzing vibration responses under various sinusoidal excitations. Using WPD and permutation entropy, their approach effectively determined both the location and magnitude of damage, showing resilience against noise and validated through finite element models and experimental data. Khanahmadi [36] proposed an effective method for identifying both single and multiple defect sites within thin-walled steel plates, commonly found in structural applications. This method, utilizing wavelet-based signal processing, applied a 1D strategy to examine 2D modal signals, achieving accurate identification of damage areas with an error margin below 5%. Both computational modeling and laboratory experiments validated its performance in locating damaged zones in plates. In a subsequent investigation, Khanahmadi et al. [37] introduced a technique for localizing defects in three-dimensional composite sandwich panels, based on modal response data. They developed the irregularity detection index (IDI), extracted from wavelet coefficients applied to fundamental and secondary mode shapes. Local maxima in the IDI signal indicated defect positions, with increased damage severity leading to a higher $IDI_{max}$ value. Variations in $IDI_{max}$ for intact regions were insignificant, and localized defect identification remained independent across different areas.

Soleimani Nezhad et al. [38] proposed a technique leveraging signal processing for damage identification in steel-braced frames, utilizing Fourier and wavelet transforms applied to structural acceleration responses. Their method, validated through laboratory tests, accurately identified both the location and timing of structural damage under seismic loading. Hassani et al. [39] conducted an extensive systematic review on data fusion techniques in SHM systems, analyzing the theoretical foundations, applications, benefits, and limitations of existing methods. They highlighted significant challenges and future trends in data fusion for SHM, proposing criteria for evaluating research and outlining a roadmap for future advancements. In a follow-up study, Hassani et al. [40] presented an enhanced damage detection approach designed to address the challenges posed by environmental and operational uncertainties. That method has integrated Gaussian smoothing, Johansen cointegration for data fusion, and an improved reptile search algorithm (IRSA), offering enhanced computational speed and accuracy. It outperformed state-of-the-art techniques in both numerical and experimental damage detection tests. Ghannadi et al. [41] proposed an efficient finite element model updating and damage detection strategy for tubular structures, employing the semi-rigidly connected frame element (S-RCFE) and optimization techniques. Their method, validated experimentally, showed effective model calibration and precise damage detection, yielding superior results with the improved grey wolf optimizer (IGWO) algorithm. Rodriguez et al. [42] introduced the single atom convolutional matching pursuit method to enhance SHM based on Lamb waves. By overcoming the limitations of conventional matching pursuit in handling dispersive signals, this approach enabled more precise signal decomposition and was validated through both numerical simulations and experimental analyses.

Among the various types of damage that can occur in composite structures, debonding defects at the concrete-steel interface in concrete-filled steel tube (CFST) columns pose a significant challenge. This type of damage can notably impact the dynamic performance of the structure, reducing its overall safety. Numerous investigations have been conducted on the detection of interfacial debonding in CFST columns. Xu et al. [43, 44] suggested a novel strategy to monitor the internal health of CFST columns, employing wavelet energy spectra and piezoelectric sensors. They embedded piezoelectric sensors on the external surface and analyzed the wavelet energy spectrum changes to detect debonding areas. Their study demonstrated that the introduced criterion was highly sensitive to debonding and capable of accurately evaluating the internal condition of the columns. In this context, a multi-scale numerical simulation was performed to analyze the response of piezoelectric sensors to wave propagation in CFST columns, confirming the significant effect of debonding on sensor behavior [45]. Furthermore, stress wave propagation analysis for rectangular and

circular sections using PZT installed on the surface and embedded in the concrete core was carried out, illustrating how the debonding between concrete and steel affects wave propagation [46–48]. Younesi et al. [49, 50] used laboratory modal data to identify debonding in CFST columns. They modeled this damage using a polystyrene layer and pinpointed the debonding location through CWT analysis. Chen et al. [51] proposed the use of the multichannel analysis of surface waves (MASW) technique to identify interfacial debonding in rectangular CFST members, validating its feasibility through mesoscale numerical simulations. Their findings highlighted that debonding strongly governs the propagation behavior of surface waves and can be reliably detected by analyzing dispersion characteristics. In a related study, Chen et al. [52] further combined surface-mounted and embedded PZT sensors with multi-physical numerical simulations to confirm that interface debonding can be efficiently detected through surface wave measurements. Mamazizi et al. [53] examined how debonding influences the reduction of mode frequencies and suggested a metric derived from detail coefficients in wavelet analysis, demonstrating its sensitivity to the damage position and intensity. Liu et al. [54] applied an ultrasonic phased array for semi-quantitative characterization of debonding in CFST columns in the Shenzhen SEG building, using total focusing method (TFM) imaging and validation via boreholes, showing high accuracy in detecting debonding. Gholhaki et al. [55] presented a damage-sensitive index derived from wavelet coefficients obtained by two-dimensional WT analysis of initial and current mode shapes, which identified clusters of irregular peaks in debonding regions, enabling damage localization. Khanahmadi et al. [56] employed two-dimensional DWT for analyzing vibration mode shapes, successfully detecting debonding regions even within the internal core of the columns. Their method was able to detect debonding at the mid and bottom boundaries of the column. Wang et al. [57] introduced a new efficient technique for detecting interfacial debonding defects in CFST structures based on wave propagation analysis using externally attached piezoelectric sensors. By introducing a normalized judgment index and a wavelet packet energy model, their study demonstrated the effectiveness of both flat and oblique measurement techniques in accurately identifying and quantifying debonding defects. Khanahmadi and Khalighi [58] utilized the concept of curvature and introduced the curvature-based modal indices, including MCI, MCSI, and MCCI, to detect debonding defect zones in CFSTs with circular cross-sections. Their findings demonstrated that these indices effectively identified debonding areas, with MCSI and MCCI particularly emphasizing irregularities and disturbances at debonding sites in contract to intact sections. Cao et al. [59] presented an approach to identifying interfacial separation in CFST columns based on acoustic signal analysis. By applying CWT to tapping-induced acoustic signals and utilizing MobileNetv2 for classification, their approach demonstrated high accuracy in both laboratory and field tests, proving effective for SHM. Yao et al. [60] proposed an ultrasonic-based Bayesian optimized-long short-term memory (BO-LSTM) method for debonding detection in CFST arch bridges, demonstrating near-perfect classification accuracy for various defect levels and providing interpretability via SHapley additive explanations (SHAP) analysis. In a subsequent study, Mirzaei et al. [61] introduced a new criterion, the modal flexibility-irregularity detection index (MFIDI), derived from the modal flexibility signal processing method, which proved effective for identifying interface debonding damages in CFSTs and cracks in beams.

This research presents an innovative approach, IDI, for effectively identifying interfacial debonding in CFST columns, particularly in critical regions such as column edges and bases. The method relies on curvature analysis of signals from initial and current mode shapes and demonstrates reliable diagnostic performance. The study highlights the potential of the proposed approach as a practical tool for SHM, and further investigations can explore its application under more complex conditions, such as dynamic loading, temperature variations, thermal effects, and other environmental influences.

Nomenclature

| | | | |
|---|---|---|---|
| $E_s$ | Elastic modulus of steel (MPa) | $\Delta\boldsymbol{\varphi}_i$ | Difference between initial and current shapes of mode i |
| $E_c$ | Elastic modulus of concrete (MPa) | $\Delta\boldsymbol{\Phi}_i$ | Interpolated $\Delta\boldsymbol{\varphi}_i$ |
| $\rho$ | Material density (kg/m$^3$) | $\boldsymbol{\kappa}$ | Central curvature matrix |
| $F_y$ | Yielding strength (MPa) | $\mathbf{s}_i$ | Signal derived from the curvature of $\Delta\boldsymbol{\Phi}_i$ |
| $F_u$ | Ultimate strength (MPa) | $\mathbf{S}_i$ | Curvature-based signal computed from $\mathbf{s}_i$ |
| $\nu$ | Poisson's ratio | H | Height of the CFST column |
| $\boldsymbol{\varphi}_i^h$ | Initial shape of mode i | h | Grid spacing along column height |
| $\boldsymbol{\varphi}_j^d$ | Current shape of mode j | $\theta$ | Angle marix between the initial and current mode shapes |
| $\omega_i$ | Natural frequency of the *i*th vibration mode | **MAC** | Modal Assurance Criterion marix |
| m, n | Number of rows and columns of the interpolated $\Delta\boldsymbol{\varphi}_i$ matrix | **IDI** | Irregularity Detection Index matrix |
| p, q | Spatial node indices in the x and y directions | | |

## Finite Element (FE) Modeling of CFST Column

A CFST composite column with a height of 3 m and an HSS steel tube measuring 30 × 20 × 1 cm was designed. The design was based on the Load and Resistance Factor Design (LRFD) method in following the provisions of AISC 360 − 16 [62], aiming to withstand a compressive load of 110 kN, a shear load of 870 kN, and a bending moment of 180 kN.m. To perform the modal analysis, the finite element modeling and simulation of the column were conducted using ABAQUS (Dassault Systèmes Simulia Corp.). In this process, the steel tube was modeled using 3D Shell elements (S4R type, i.e., 4-node doubly curved thin or thick shell element with reduced integration, hourglass control, and finite membrane strains), whereas the concrete core was modeled using solid elements (C3D8R type, i.e., 8-node linear brick element, with reduced integration and hourglass control), consistent with their respective element behaviors. Additionally, the column's boundary conditions were defined as fully fixed at both ends. The steel material properties are provided in Table 1.

For concrete, the material density is set to 2400 kg/m$^3$, the yield strength is 30 MPa, and the Poisson's ratio is 0.20. Using these characteristics, the elastic modulus of concrete is determined through Eq. (2) [62].

$$E_c = 0.043 w_c^{1.5} \sqrt{f'_c} = 0.043\,(2400)^{1.5}\,\sqrt{30} = 27691 MPa \qquad (1)$$

Figure 1 illustrates the FE representation of the CFST composite column with fully fixed supports, incorporating both undamaged and debonded states corresponding to cases D1, D2, and D3. The debonding regions are clearly highlighted in Fig. 1, with detailed descriptions provided in Table 2. To simulate debonding, the elastic modulus of concrete is reduced within a 3 mm layer at the junction with the steel.

## Modal Dynamic Analysis of CFST Column

In this analysis, a modal response of the CFST composite column was evaluated under two conditions: an undamaged state and with interfacial separation, assuming a 45% deterioration level in the affected zones. The simulation framework incorporated a 4-node discretized steel and an 8-node meshed concrete, each measuring 5 cm.

Table 3 outlines the computed frequency metrics for the first four modes, revealing that the presence of debonding results in a decline in resonance values across all modes. Furthermore, when contrasting cases D1 and D2, as well as D1, D2, and D3 collectively, it is observed that a rise in the number of debonded sections exacerbates the reduction in frequency. These results emphasize the critical importance of detecting early-stage debonding in order to prevent structural deterioration and reduce the risk of potential failures by implementing proactive measures.

Figure 2 displays the mode shapes in their intact condition. To analyze the influence of interfacial debonding on these mode shapes, the modal assurance criterion (MAC) is applied, following the formulation in Eq. (2) [63–66]:

$$\mathbf{MAC}\,(i,j) = \left(\left\{\boldsymbol{\varphi}_i^h\,(:)\right\}^T \left\{\boldsymbol{\varphi}_i^h\,(:)\right\}\right)^{-1} \left(\left\{\boldsymbol{\varphi}_i^h\,(:)\right\}^T \left\{\boldsymbol{\varphi}_j^d\,(:)\right\}\right)^2 \left(\left\{\boldsymbol{\varphi}_j^d\,(:)\right\}^T \left\{\boldsymbol{\varphi}_j^d\,(:)\right\}\right)^{-1} \qquad (2)$$

where $\left\{\boldsymbol{\varphi}_{\mathrm{i}}^{\mathrm{h}}\,(:)\right\}$ and $\left\{\boldsymbol{\varphi}_{\mathrm{j}}^{\mathrm{d}}\,(:)\right\}$ denote the initial mode shape i (in its intact condition) and the corresponding secondary mode shape j (in the presence of debonding), respectively. $\mathbf{MAC}\,(\mathrm{i},\mathrm{j})$ forms a matrix that assesses the similarity between these mode shapes. The **MAC** values, ranging within $0 < \mathbf{MAC}\,(\mathrm{i},\mathrm{j}) \leq 1$, quantify their resemblance under the intact and the interfacial debonding defect conditions. If the **MAC** matrix is asymmetric and its diagonal elements deviate from 1, it signals structural deterioration.

In this study, **MAC** matrix is employed to assess the impact of debonding defects on mode shapes. Tables 4, 5 and 6 present its effects on **MAC** matrices, with emphasis on asymmetry and non-unity diagonal values.

## Curvature-Driven Damage-Sensitive Feature Extraction Method

This research presents a novel approach for detecting interfacial debonding defect zones in CFST columns. The method relies on the curvature analysis of initial and current vibration mode shapes and introduces a novel irregularity detection index (IDI) as an effective evaluation and diagnostic criterion. In this approach, after computing the IDI, irregularities and perturbations are assigned to the corresponding nodes. The diagnostic performance of this index reveals that the magnitude of irregularities and perturbations in debonding regions is significantly higher than in other areas. More specifically, irregularity peaks in debonding regions are more pronounced compared to those observed

**Table 1** Characteristics of the steel material

| $E_s$ (MPa) | ρ $\left(\mathrm{kg/m^3}\right)$ | $\nu$ | G (MPa) | $F_y$ (MPa) | $F_u$ (MPa) |
|---|---|---|---|---|---|
| 210,000 | 7850 | 0.30 | 80769.23 | 235 | 360 |

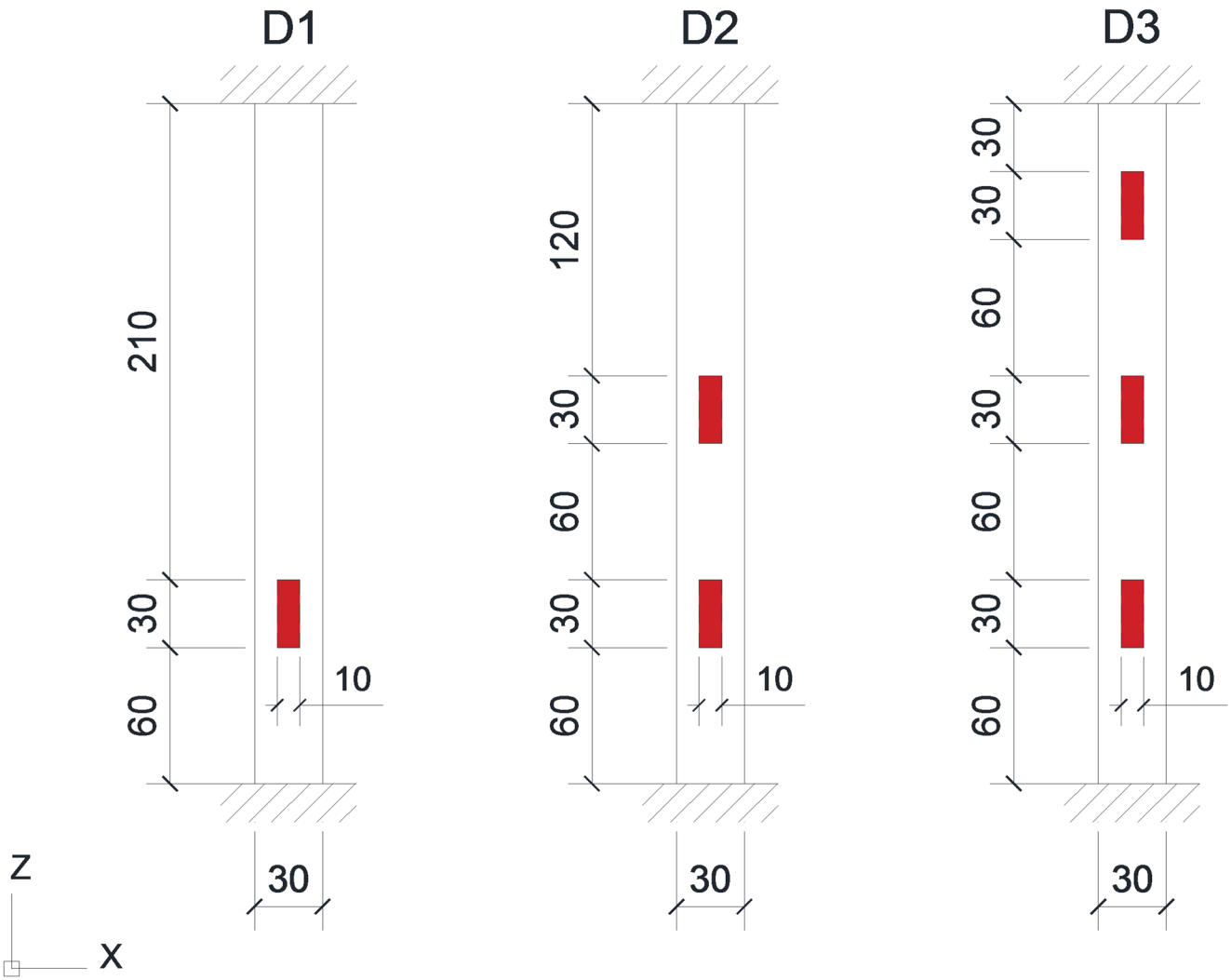


**Fig. 1** CFST column showing debonding regions in D1, D2 and D3 debonding cases

**Table 2** CFST column with debonding regions in D1, D2 and D3 debonding cases [56]

| Debonding Case | Number of Debonding Sites | Debonding Region (cm) |
|---|---|---|
| D1 | 1 | 60–90 |
| D2 | 2 | 60–90 |
| | | 150–180 |
| D3 | 3 | 60–90 |
| | | 150–180 |
| | | 240–270 |

**Table 3** Computed natural frequency values of the CFST column in its intact condition and under D1, D2 and D3 debonding cases

| Debonding Case | Natural frequency (Hz) | | | |
|---|---|---|---|---|
| | $\omega_1$ | $\omega_2$ | $\omega_3$ | $\omega_4$ |
| No-Debonding (Intact) | 113.98 | 294.94 | 538.25 | 824.36 |
| D1 | 113.97 | 294.91 | 538.21 | 824.33 |
| D2 | 113.96 | 294.90 | 538.15 | 824.27 |
| D3 | 113.96 | 294.89 | 538.11 | 824.20 |

in intact areas, thereby facilitating the identification of debonding zones. Subsequently, the computation process of the IDI and the damage detection procedure based on this index are elaborated in Steps 1 to 7.

**Step 1:** The angle matrix between the initial and current vibration mode shapes is computed using Eq. (3) [56, 67]. If the angle matrix is asymmetric or its main diagonal elements are nonzero, it indicates that the structure has sustained damage. In this case, it is necessary to detect the locations of the damaged areas. Otherwise, if the matrix exhibits symmetry and all diagonal values are zero, the structure is considered healthy, and the SHM process is concluded.

$$\theta_{(i,j)} = \frac{180^{\circ}}{\pi} arccos\left(\left(\left(\sum_{k=1}^{m}\sum_{r=1}^{n}\left(\varphi_i^{h}(k,r)\right)^2\right)\left(\sum_{k=1}^{m}\sum_{r=1}^{n}\left(\varphi_j^{d}(k,r)\right)^2\right)\right)^{-\frac{1}{2}}\left(\sum_{k=1}^{m}\sum_{r=1}^{n}\left(\varphi_i^{h}(k,r)\,\varphi_j^{d}(k,r)\right)\right)\right) \quad (3)$$

**Step 2:** In Eq. (3), $\boldsymbol{\varphi}_i^{h}$ represents the primary mode shape i (the undamaged mode shape), while $\boldsymbol{\varphi}_j^{d}$ denotes the

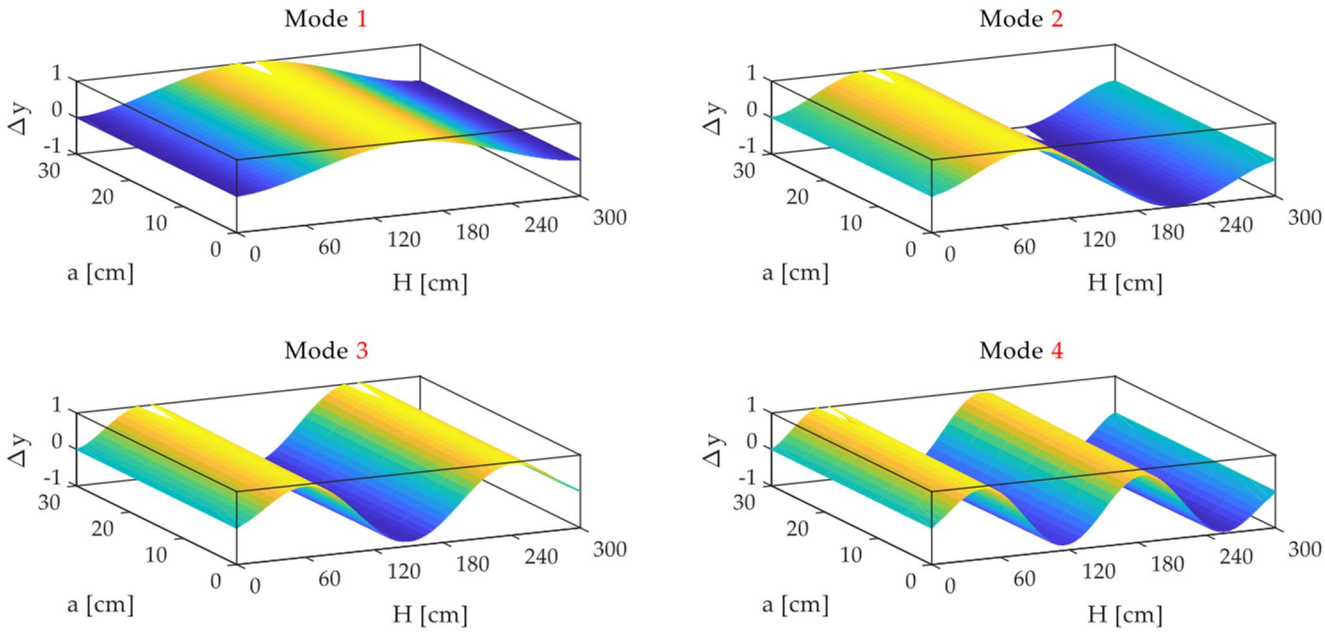


**Fig. 2** The first four vibration mode shapes of the intact column

**Table 4** **MAC** matrix of the intact state and the debonding scenario D1

| MAC (i, j) | | Mode Number (D1 Debonding Case) | | | |
|---|---|---|---|---|---|
| | | 1 | 2 | 3 | 4 |
| Mode Number (Intact Condition) | 1 | 9.99999999453338E-01 | 4.04356133897832E-10 | 3.89508585364601E-05 | 2.87014631606563E-11 |
| | 2 | 4.29059729346115E-10 | 9.99999979789052E-01 | 1.84234792625137E-08 | 9.95502672407531E-05 |
| | 3 | 3.90239332545775E-05 | 1.63332887592620E-08 | 9.99999965167971E-01 | 6.31301357149473E-09 |
| | 4 | 1.95529950823128E-11 | 9.97604306535083E-05 | 5.67881111607699E-09 | 9.99999971260689E-01 |

**Table 5** **MAC** matrix of the intact state and the debonding scenario D2

| MAC (i, j) | | Mode Number (D2 Debonding Case) | | | |
|---|---|---|---|---|---|
| | | 1 | 2 | 3 | 4 |
| Mode Number (Intact Condition) | 1 | 9.99999997557646E-01 | 3.28826550957272E-10 | 3.95231007414392E-05 | 1.17291517458193E-10 |
| | 2 | 2.57634033764846E-10 | 9.99999964910993E-01 | 3.44260769705408E-08 | 1.00310933172564E-04 |
| | 3 | 3.84836158777469E-05 | 3.01361747541845E-08 | 9.99999936358070E-01 | 1.07364974801626E-09 |
| | 4 | 1.34696154530670E-10 | 9.89829554337910E-05 | 9.03522498538246E-10 | 9.99999942900959E-01 |

**Table 6** **MAC** matrix of the intact state and the debonding scenario D3

| MAC (i, j) | | Mode Number (D3 Debonding Case) | | | |
|---|---|---|---|---|---|
| | | 1 | 2 | 3 | 4 |
| Mode Number (Intact Condition) | 1 | 9.99999996025683E-01 | 6.25681039026529E-10 | 3.96736053424146E-05 | 7.35858837678770E-10 |
| | 2 | 5.57787381338744E-10 | 9.99999981090003E-01 | 1.55554990580540E-08 | 1.00102018045353E-04 |
| | 3 | 3.83659843467438E-05 | 1.33356482773159E-08 | 9.99999929137751E-01 | 3.43496419551722E-08 |
| | 4 | 5.12799900211615E-10 | 9.93945221598553E-05 | 3.22025196421117E-08 | 9.99999917784869E-01 |

secondary mode shape j (the damaged mode shape). If the structure is determined to be damaged and $\theta\ (i,i) \geq 90^{\circ}$, then $-\boldsymbol{\varphi}_i^{d}$ is substituted for $\boldsymbol{\varphi}_i^{d}$.

**Step 3:** The secondary mode shape i is subtracted from its corresponding primary mode shape (Eq. (4)). Subsequently, interpolation is performed on the resulting data (Eq. (5)). (In this study, interpolation is conducted as a single-step averaging process.)

$$\Delta \boldsymbol{\varphi}_i = \boldsymbol{\varphi}_i^{h} - \boldsymbol{\varphi}_i^{d} \tag{4}$$

$$\Delta \boldsymbol{\Phi}_i = \text{interp2}\left(\Delta \boldsymbol{\varphi}_i,\ 1\right) \tag{5}$$

**Step 4:** The central curvature for $\Delta \boldsymbol{\Phi}_i$ at coordinates $(p,\ q)$ is computed using Eq. (6). Then, the signal $s_i$ is defined using Eq. (7).

$$\kappa_{\Delta \boldsymbol{\Phi}_i}(p,q) = \left(\frac{\partial}{\partial z}\left(\frac{\partial \Delta \boldsymbol{\Phi}_i}{\partial z}\right)\right)_{p,q} \approx \frac{1}{h^2} \left(\left(\Delta \boldsymbol{\Phi}_i(p,q+1) - \Delta \boldsymbol{\Phi}_i(p,q)\right) - \left(\Delta \boldsymbol{\Phi}_i(p,q) - \Delta \boldsymbol{\Phi}_i(p,q-1)\right)\right) \tag{6}$$

$$s_i(p,q) = \left|\kappa_{\Delta \boldsymbol{\Phi}_i}(p,q)\right| \left(\left(\left|\kappa_{\Delta \boldsymbol{\Phi}_i}(p,q)\right| - \left(\frac{1}{mn}\sum_{k=1}^{m}\left(\sum_{r=1}^{n}\left|\kappa_{\Delta \boldsymbol{\Phi}_i}(k,r)\right|\right)\right)\right) \geq 0\right) \tag{7}$$

In Eqs. (6) and (7), $[m,n] = \text{size}\left(\Delta \boldsymbol{\Phi}_i\right)$ and h is computed using Eq. (8). Here, H denotes the height of the column.

$$\mathbf{a} = \text{linspace}\left(0, H, n\right) \quad \rightarrow \quad h = \mathbf{a}(2) - \mathbf{a}(1) \tag{8}$$

**Step 5:** The curvature of the signal $s_i$ is determined using Eq. (9). Subsequently, the signal $S_i$ is defined by Eq. (10).

$$\kappa_{s_i}(p,q) = \left(\frac{\partial}{\partial z}\left(\frac{\partial s_i}{\partial z}\right)\right)_{p,q} \approx \frac{1}{h^2}\left(\left(s_i(p,q+1) - s_i(p,q)\right) - \left(s_i(p,q) - s_i(p,q-1)\right)\right) \tag{9}$$

$$S_i(p,q) = \left|\kappa_{s_i}(p,q)\right| \left(\left(\left|\kappa_{s_i}(p,q)\right| - \left(\frac{1}{mn}\sum_{k=1}^{m}\left(\sum_{r=1}^{n}\left|\kappa_{s_i}(k,r)\right|\right)\right)\right) \geq 0\right) \tag{10}$$

**Step 6:** The IDI is proposed as a criterion for determining irregularities to evaluate the structural health of the CFST column and identify the interfacial debonding regions, using Eq. (11)

$$\mathbf{IDI}(p,q) = \left(\sum_{i=1}^{N}\left(\frac{S_i(p,q)}{\max\left(\max\left(S_i\right)\right)}\right)\right)\left(\left(\sum_{i=1}^{N}\left(\frac{S_i(p,q)}{\max\left(\max\left(S_i\right)\right)}\right)\right) - \left(\frac{1}{mn}\sum_{k=1}^{m}\left(\sum_{r=1}^{n}\left(\sum_{i=1}^{N}\left(\frac{S_i(k,r)}{\max\left(\max\left(S_i\right)\right)}\right)\right)\right)\right) \geq 0\right) \tag{11}$$

In this context, N indicates the total number of vibration modes. (In this study, the initial and current shapes of the first four vibration modes are used in the calculation of the **IDI**.)

**Step 7:** The identification and detection of debonding regions are performed by assigning the $\mathbf{IDI}(p,q)$ as the irregularity to the node with coordinates $(p,q)$.

## Detection and Localization of Interfacial Debonding Zones

Following Steps 1 through 7, the structural damage identification algorithm was executed in MATLAB (MathWorks, Inc.). Initially, the angle matrix between the initial mode shape i and the damaged mode shape j under debonding conditions D1, D2, and D3 was computed, with the corresponding value listed in Tables 7, 8 and 9. The results reveal that these matrices exhibit asymmetry, and their diagonal elements show nonzero angles. This asymmetry is related to the influence of interfacial debonding defects on the vibration mode shapes in the current state of the structure. Additionally, the presence of nonzero diagonal elements signifies a discrepancy between the initial and secondary shapes of mode i, which is attributed to structural damage in the column.

As the algorithm progresses through the subsequent steps, the irregularity signal (i.e., **IDI**) is calculated for

**Table 7** The angle between the primary and secondary vibration mode shapes (debonding scenario D1)

| $\theta\ (i,j)$ | | Mode Number (D1 Debonding Damage Scenario) | | | |
|---|---|---|---|---|---|
| | | 1 | 2 | 3 | 4 |
| Mode Number (Intact Condition) | 1 | 1.33962145612951E-03 | 9.00011521383962E+01 | 8.96424111495481E+01 | 9.00003069549568E+01 |
| | 2 | 8.99988131891455E+01 | 8.14546675348973E-03 | 9.00077769348128E+01 | 9.05716774392107E+01 |
| | 3 | 8.96420758706772E+01 | 8.99926774987642E+01 | 1.06933066870054E-02 | 8.99954475939236E+01 |
| | 4 | 9.00002533548823E+01 | 8.94277194166069E+01 | 8.99956823111242E+01 | 1.79990286834056E+02 |

**Table 8** The angle between the primary and secondary vibration mode shapes (debonding scenario D2)

| $\theta\ (i,j)$ | | Mode Number (D2 Debonding Damage Scenario) | | | |
|---|---|---|---|---|---|
| | | 1 | 2 | 3 | 4 |
| Mode Number (Intact Condition) | 1 | 2.83156703871739E-03 | 8.99989610226712E+01 | 8.96397939541697E+01 | 9.00006205202158E+01 |
| | 2 | 9.00009196535446E+01 | 1.07326798224069E-02 | 9.00106308111347E+01 | 8.94261425439831E+01 |
| | 3 | 8.96445624116559E+01 | 8.99900535822105E+01 | 1.44542081874777E-02 | 8.99981226123970E+01 |
| | 4 | 8.99993350327892E+01 | 8.94299538646366E+01 | 9.00017222338390E+01 | 1.36910589861516E-02 |

**Table 9** The angle between the primary and secondary vibration mode shapes (debonding scenario D3)

| θ (i, j) | | Mode Number (D3 Debonding Damage Scenario) | | | |
|---|---|---|---|---|---|
| | | 1 | 2 | 3 | 4 |
| Mode Number (Intact Condition) | 1 | 3.61205073243829E-03 | 8.99985668253112E+01 | 8.96391087615971E+01 | 9.00015542464623E+01 |
| | 2 | 9.00013531843768E+01 | 7.87895035739555E-03 | 9.00071460262629E+01 | 8.94267404548548E+01 |
| | 3 | 8.96451060612260E+01 | 8.99933834789321E+01 | 1.52521160873987E-02 | 8.99893809970325E+01 |
| | 4 | 8.99987025321703E+01 | 8.94287699415701E+01 | 9.00102817623539E+01 | 1.64285227161150E-02 |

each of the interfacial debonding cases D1, D2, and D3. By assigning irregularity values to the nodes, it becomes evident that the peak magnitudes associated with deviations and disturbances in the defect areas—as well as their adjacent zones—are considerably more pronounced than those in undamaged positions. This trend is clearly demonstrated in Figs. 3, 4 and 5.

## Identification of Debonding Regions at Mid-Span and End Under Edge Boundary Conditions

A significant challenge in SHM and damage identification techniques relying on signal analysis and feature extraction is the precise detection of damage in boundary edge regions. This issue is particularly critical in structural components like beams and columns, where damage near the supports requires special consideration. The approach introduced in this work has shown both excellent diagnostic accuracy and practical effectiveness.

To illustrate this, consider the following damage scenarios:

D4: Representing a debonding defect zone located at the column base under double-edge boundary conditions.
D5: Involving a mid-span debonding defect zone subjected to single-edge boundary conditions.
D6: Depicting a combined case of both D4 and D5.

The precise dimensions for these cases are outlined in Table 10 and illustrated in Fig. 6. The severity of debonding, defined as a 45% decrease in the elastic modulus of the concrete-steel interface, was analyzed through a frequency study of the column. The frequency values obtained are provided in Table 11.

By comparing damage cases D4 and D5, it becomes apparent that, despite the identical debonding area, depth, and severity, the defect near the column base results in a greater frequency reduction than damage in the mid-span region. This finding suggests that, under equivalent conditions, debonding at the base of the column poses a greater risk to structural stability.

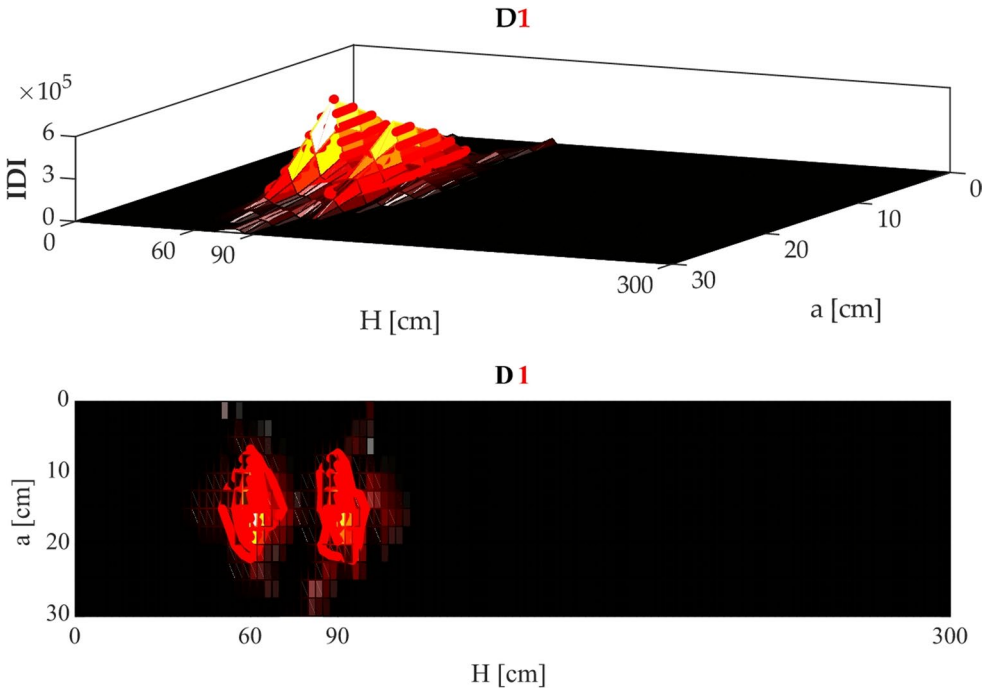


**Fig. 3** Surface plot of the **IDI** showing peaks of irregularities and disturbances for the debonding state D1

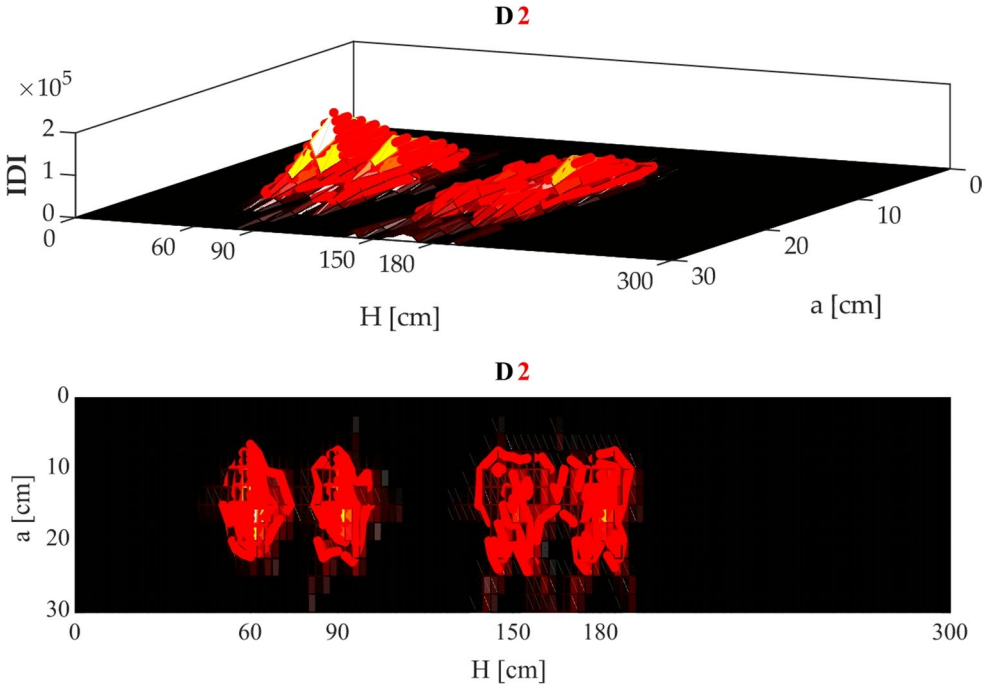


**Fig. 4** Surface plot of the **IDI** showing peaks of irregularities and disturbances for the debonding state D2

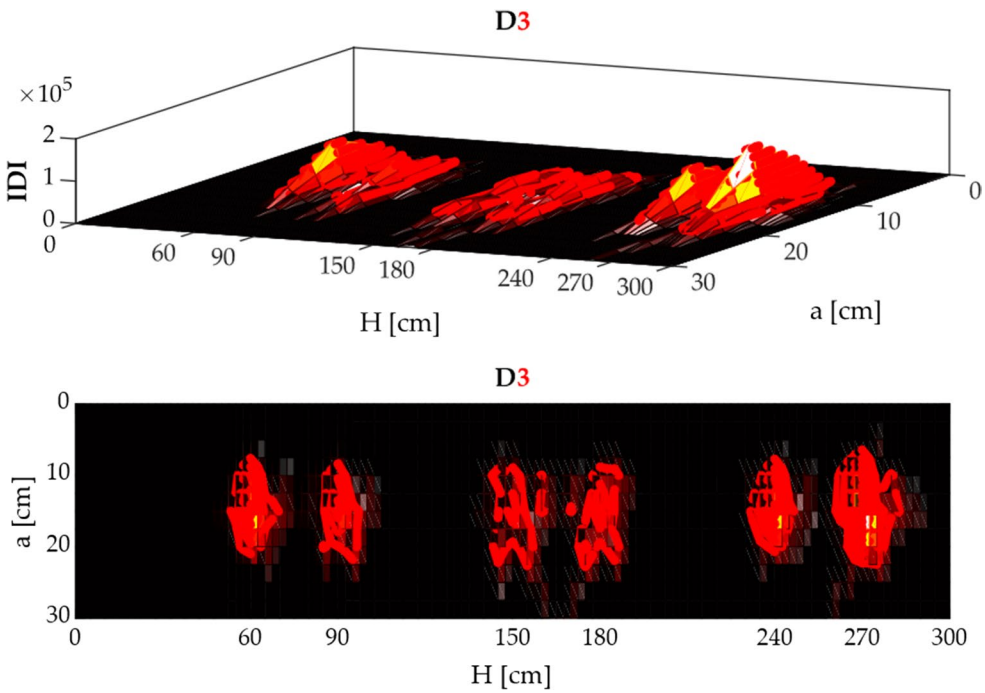


**Fig. 5** Surface plot of the **IDI** showing peaks of irregularities and disturbances for the debonding state D3

The angle matrices, measured in degrees, are listed in Tables 12, 13 and 14. The term "angle between intact and current mode shapes" denotes the angular difference between corresponding vectors of distinct mode shapes. As an illustration, in Table 13, the calculated angles for the second and fourth modes are 179.996° and 179.952°, respectively. These values indicate that, as a consequence of the incurred damage, the modal displacement in the present state occurs in a reversed direction compared to its primary condition (refer to Fig. 7).

The proposed algorithm presented in Section Curvature-Driven Damage-Sensitive Feature Extraction Method has been implemented for the debonding cases D4, D5, and D6. The results obtained, which are displayed in Figs. 8, 9 and 10, demonstrate that the **IDI** introduced in this study has high accuracy and efficiency in identifying the debonding regions

**Table 10** CFST column with debonding zones in cases D4, D5, and D6 [56]

| Debonding Case | Number of Debonding Zones | Debonding Zone (cm) | Edge Boundary Conditions |
|---|---|---|---|
| D4 | 1 | 0–30 | Column's base with two edge boundaries |
| D5 | 1 | 120–150 | Mid-span with one edge boundary |
| D6 | 2 | 0–30 | Column's base with two edge boundaries |
| | | 120–150 | Mid-span with one edge boundary |

**Table 11** Frequency values in intact condition and interfacial debonding cases D4, D5, and D6

| Debonding Case | Natural frequency (Hz) | | | |
|---|---|---|---|---|
| | $\omega_1$ | $\omega_2$ | $\omega_3$ | $\omega_4$ |
| D4 | 113.95 | 294.90 | 538.19 | 824.27 |
| D5 | 113.96 | 294.93 | 538.19 | 824.30 |
| D6 | 113.94 | 294.89 | 538.13 | 824.21 |

between the concrete and the steel tube. This effectiveness is particularly evident in situations where debonding occurs at the boundary edges or column base regions.

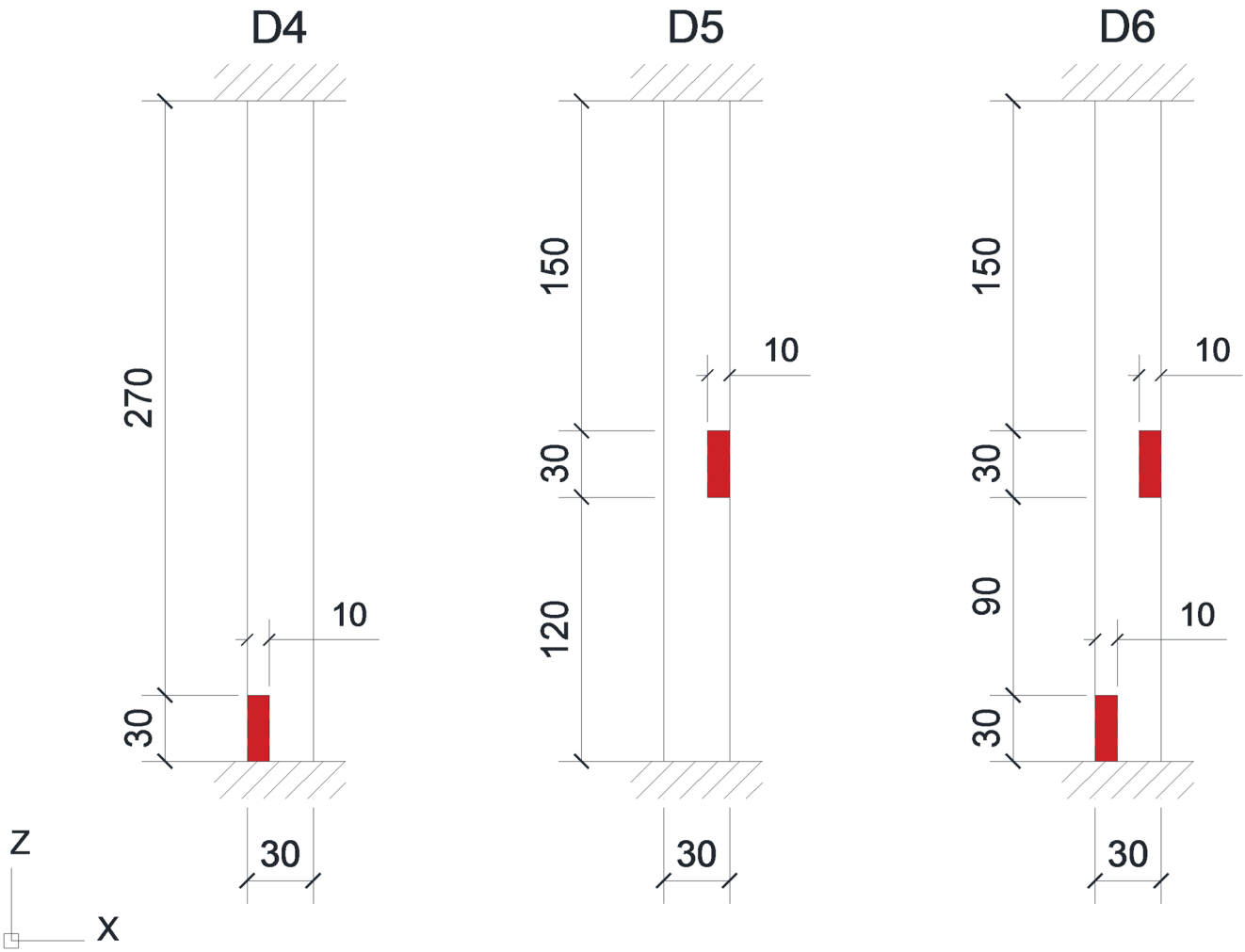


**Fig. 6** Representation of the CFST column showing interface debonding in cases D4, D5, and D6

**Table 12** The angle between the intact and current mode shapes (for the debonding defect case D4)

| θ (i, j) | | Mode Number (D4 Debonding Case) | | | |
|---|---|---|---|---|---|
| | | 1 | 2 | 3 | 4 |
| Mode Number (Intact Condition) | 1 | 1.24423031681371E-02 | 9.00287186678087E+01 | 8.96360666897861E+01 | 9.00042256215792E+01 |
| | 2 | 8.99884895689767E+01 | 3.35641494588853E-02 | 9.00275481884874E+01 | 9.06246852632517E+01 |
| | 3 | 8.96383328321347E+01 | 8.99896127215797E+01 | 3.55326505206456E-02 | 8.99734013667792E+01 |
| | 4 | 8.99983330940607E+01 | 8.94236065576838E+01 | 8.99887675394316E+01 | 1.79912492712573E+02 |

The present research has successfully introduced the **IDI** as an effective and valuable diagnostic tool for detecting and evaluating damage-induced changes in the mid and end positions of the column. One of the major challenges in damage detection techniques relying on signal processing is the precise detection of changes occurring at the boundary edges. This study has addressed this issue by employing an innovative and effective approach, providing an appropriate and optimal solution.

## Numerical Evaluation of IDI Sensitivity To Random Noise

To evaluate the sensitivity of the proposed IDI method to noise in experimental data, a numerical study was conducted to simulate laboratory-like conditions. Assuming that noise affects the modal displacements of all nodes, this effect can be considered using Eqs. (12) and (13) [68]:

$$\mathbf{R} = \mathrm{a} + (\mathrm{b} - \mathrm{a}) \times \mathbf{rand}\,(\mathrm{N_r}, \mathrm{N_c}) \tag{12}$$

**Table 13** The angle between the intact and current mode shapes (for the debonding defect case D5)

| θ (i, j) | | Mode Number (D5 Debonding Case) | | | |
|---|---|---|---|---|---|
| | | 1 | 2 | 3 | 4 |
| Mode Number (Intact Condition) | 1 | 2.17959348937273E-03 | 8.99999871972691E+01 | 8.96412486496393E+01 | 8.99993976476691E+01 |
| | 2 | 8.99990134489578E+01 | 1.79996217974802E+02 | 8.99997162460496E+01 | 9.06019942564190E+01 |
| | 3 | 8.96437828095910E+01 | 8.99993402112987E+01 | 8.89908803505611E-03 | 9.00053848593858E+01 |
| | 4 | 9.00004923340994E+01 | 9.05696183847927E+01 | 8.99970469631731E+01 | 1.79955287316089E+02 |

**Table 14** The angle between the intact and current mode shapes (for the debonding defect case D6)

| θ (i, j) | | Mode Number (D6 Debonding Case) | | | |
|---|---|---|---|---|---|
| | | 1 | 2 | 3 | 4 |
| Mode Number (Intact Condition) | 1 | 1.29882807146756E-02 | 8.99712735622266E+01 | 8.96350426407479E+01 | 9.00036149268941E+01 |
| | 2 | 8.99875051932541E+01 | 1.79966710917849E+02 | 9.00272728316289E+01 | 9.06546556969873E+01 |
| | 3 | 8.96398494679875E+01 | 9.00097295229569E+01 | 3.62285236551541E-02 | 8.99787960124317E+01 |
| | 4 | 8.99988270884238E+01 | 9.05740924391040E+01 | 8.99858148630420E+01 | 1.79873443528994E+02 |

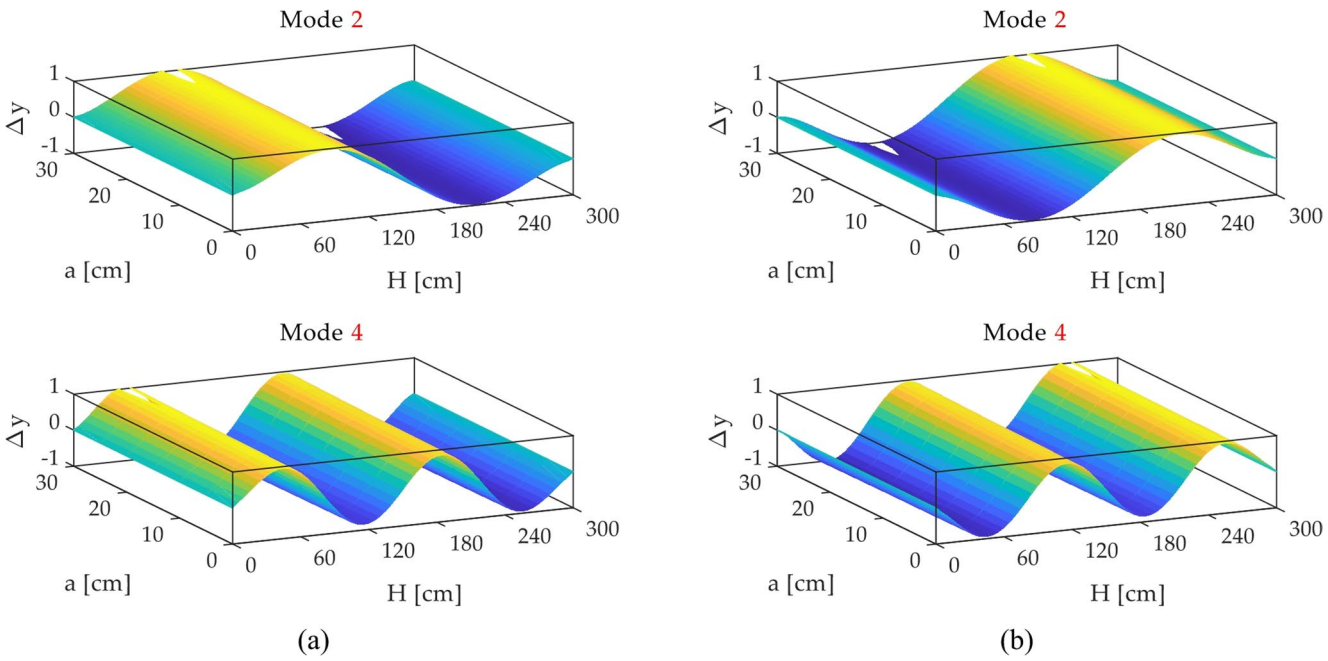


**Fig. 7** Primary and secondary shapes of vibration modes 2 and 4 : (**a**) Intact state, (**b**) Damage scenario D5

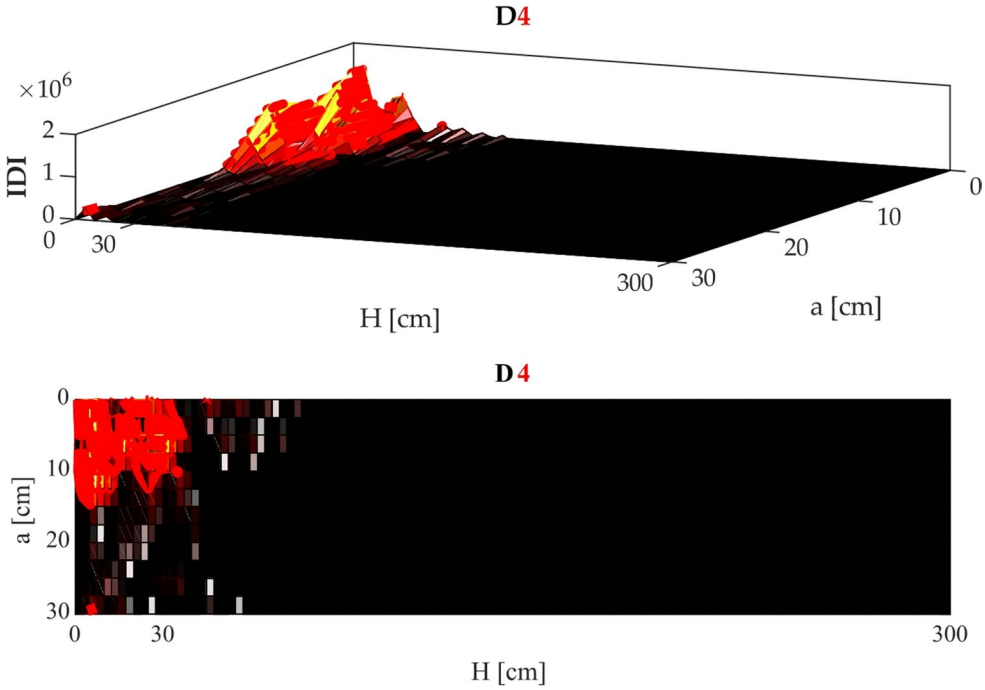


**Fig. 8** Surface plot of the **IDI** showing peaks of irregularities and disturbances for the damaged state D4, including a debonding region located at the column base with two boundary edges

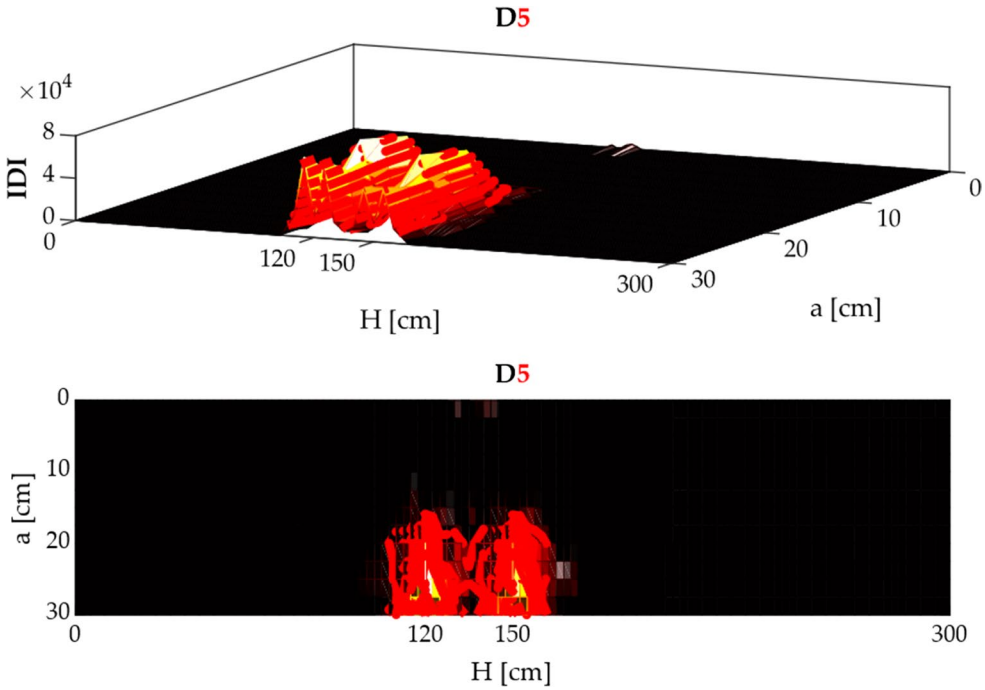


**Fig. 9** Surface plot of the **IDI** showing peaks of irregularities and disturbances for the damaged state D5, including a debonding region located at the midsection of the column with one boundary edge

$$\boldsymbol{\varphi}_{\mathrm{i}}^{\mathrm{d,\,Noise}} = \boldsymbol{\varphi}_{\mathrm{i}}^{\mathrm{d}} + \left(\frac{\mathrm{Noise}}{100}\right)\left[\boldsymbol{\varphi}_{\mathrm{i}}^{\mathrm{d}}(\mathrm{k}_1,\mathrm{k}_2)\,\mathbf{R}\,(\mathrm{k}_1,\mathrm{k}_2)\right]_{\mathrm{N_r}\times\mathrm{N_c}} \tag{13}$$

where $\alpha = -b = -1$ and $[N_r,\ N_c] = \text{size}\left(\phi_i^d\right)$.

It should be noted that in each run of the damage detection code, a new random matrix **R** is generated; consequently, the pattern of irregularities and disturbances by **IDI** changes with each execution. Figure 11 shows a random matrix **R**, and the results presented in Fig. 12 correspond to this same matrix. The analysis was conducted for noise levels of 0.0020 and 0.0025. It is observed that the aggregation of irregularities exhibits pronounced peaks at the debonding locations, indicating that the IDI method is minimally sensitive to data noise and maintains its diagnostic capability under laboratory-like conditions.

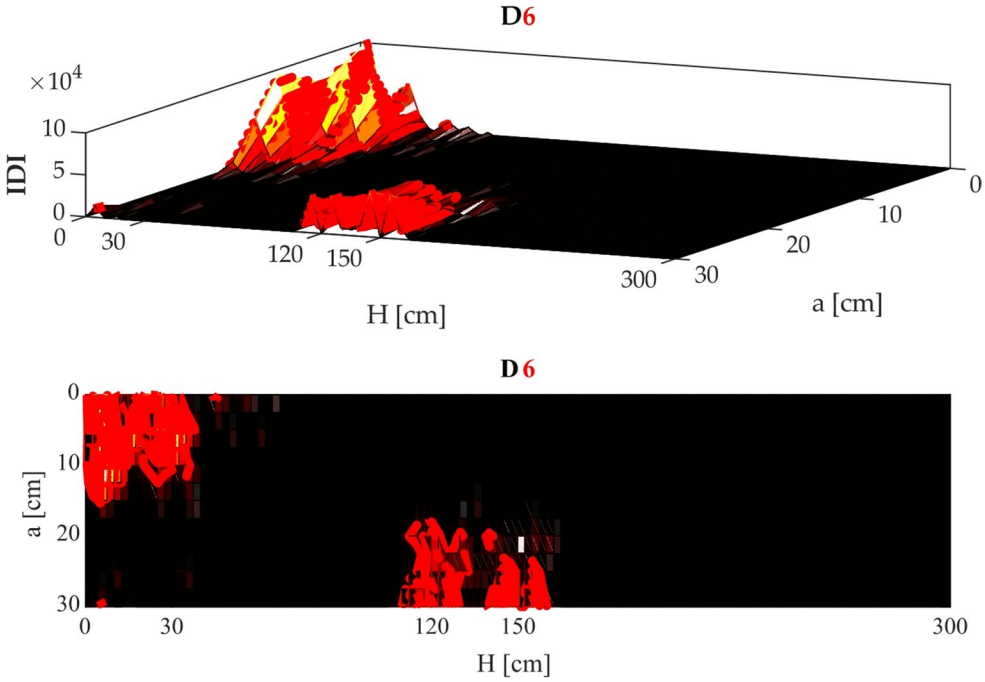


**Fig. 10** Surface plot of the **IDI** showing peaks of irregularities and disturbances for the damaged state D6, including a debonding region located at the column base with two boundary edges and a debonding region located at the midsection of the column with one boundary edge

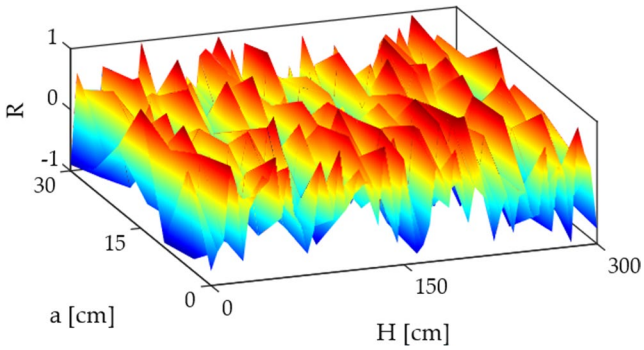


**Fig. 11** A sample random matrix **R** created to represent noise effects on the mode shapes in the damaged CFST column

It should be noted that, with increased damage severity at the damaged locations and considering equal noise levels and the same random matrix R, the diagnostic performance of a signal-processing-based method for identifying locations with higher damage severity is improved [68].

## Validation of IDI Diagnostic Performance Using a Novel Wavelet-Based Feature Extraction Method

WT is a powerful mathematical tool for signal processing in both time and frequency domains and has been widely employed in numerous studies for various approaches to structural damage identification. Comparing a novel damage detection method with existing techniques in this domain can effectively illustrate and demonstrate the diagnostic capabilities of the new approach. To this end, a mode shape sensitivity-based wavelet feature extraction method was specifically selected for detecting interface debonding in CFSTs. The proposed index in the referred study is defined using Eqs. (14) and (15) [56].

$$\mathbf{IDI}_{\mathrm{T}} = \sum_{\mathrm{i}=1}^{\mathrm{N}} \left(\mathbf{IDI}_{\mathrm{i}}^{\mathrm{H}} + \mathbf{IDI}_{\mathrm{i}}^{\mathrm{V}} + \mathbf{IDI}_{\mathrm{i}}^{\mathrm{D}}\right) \tag{14}$$

$$\mathrm{NIDI}_{\mathrm{T}} = \left(\frac{1}{m_1 n_1}\sum_{k_1=1}^{m_1}\sum_{k_2=1}^{n_1}\left(\mathbf{IDI}_{\mathrm{T}}(k_1,k_2) - \left(\frac{1}{m_1 n_1}\sum_{k_1=1}^{m_1}\sum_{k_2=1}^{n_1}\mathbf{IDI}_{\mathrm{T}}(k_1,k_2)\right)\right)^2\right)^{-\frac{1}{2}}\left|\mathbf{IDI}_{\mathrm{T}} - \left(\frac{1}{m_1 n_1}\sum_{k_1=1}^{m_1}\sum_{k_2=1}^{n_1}\mathbf{IDI}_{\mathrm{T}}(k_1,k_2)\right)\right| \tag{15}$$

In Eq. (14), $\mathbf{IDI}_{\mathrm{i}}^{\mathrm{H}}$, $\mathbf{IDI}_{\mathrm{i}}^{\mathrm{V}}$, and $\mathbf{IDI}_{\mathrm{i}}^{\mathrm{D}}$ represent the irregularity index matrices along the horizontal, vertical, and diagonal directions, respectively, and are defined using Eqs. (16) to (18) [56]. Here, N denotes the number of vibration modes, and $[\mathrm{m}_1, \mathrm{n}_1] = \mathrm{size}\,(\mathbf{IDI}_{\mathrm{T}})$.

$$\mathbf{IDI}_{\mathrm{i}}^{\mathrm{H}}(k_1,k_2) = \left|\mathbf{cH}_{\mathrm{i}}(k_1,k_2)\left(\left(\mathbf{cH}_{\mathrm{i}}(k_1,k_2) \geq \mathrm{I}_{\mathrm{f}}^{\mathrm{H}} \times \min\left(\left[\frac{\max(\mathbf{cH}_{\mathrm{i}}(:))}{-\min(\mathbf{cH}_{\mathrm{i}}(:))}\right]\right)\right) - \left(\mathbf{cH}_{\mathrm{i}}(k_1,k_2) \leq \mathrm{I}_{\mathrm{f}}^{\mathrm{H}} \times \max\left(\left[\frac{-\max(\mathbf{cH}_{\mathrm{i}}(:))}{\min(\mathbf{cH}_{\mathrm{i}}(:))}\right]\right)\right)\right)\right| \tag{16}$$

$$\mathbf{IDI}_{\mathrm{i}}^{\mathrm{V}}(k_1,k_2) = \left|\mathbf{cV}_{\mathrm{i}}(k_1,k_2)\left(\left(\mathbf{cV}_{\mathrm{i}}(k_1,k_2) \geq \mathrm{I}_{\mathrm{f}}^{\mathrm{V}} \times \min\left(\left[\frac{\max(\mathbf{cV}_{\mathrm{i}}(:))}{-\min(\mathbf{cV}_{\mathrm{i}}(:))}\right]\right)\right) - \left(\mathbf{cV}_{\mathrm{i}}(k_1,k_2) \leq \mathrm{I}_{\mathrm{f}}^{\mathrm{V}} \times \max\left(\left[\frac{-\max(\mathbf{cV}_{\mathrm{i}}(:))}{\min(\mathbf{cV}_{\mathrm{i}}(:))}\right]\right)\right)\right)\right| \tag{17}$$

$$\mathbf{IDI}_{\mathrm{i}}^{\mathrm{D}}(k_1,k_2) = \left|\mathbf{cD}_{\mathrm{i}}(k_1,k_2)\left(\left(\mathbf{cD}_{\mathrm{i}}(k_1,k_2) \geq \mathrm{I}_{\mathrm{f}}^{\mathrm{D}} \times \min\left(\left[\frac{\max(\mathbf{cD}_{\mathrm{i}}(:))}{-\min(\mathbf{cD}_{\mathrm{i}}(:))}\right]\right)\right) - \left(\mathbf{cD}_{\mathrm{i}}(k_1,k_2) \leq \mathrm{I}_{\mathrm{f}}^{\mathrm{D}} \times \max\left(\left[\frac{-\max(\mathbf{cD}_{\mathrm{i}}(:))}{\min(\mathbf{cD}_{\mathrm{i}}(:))}\right]\right)\right)\right)\right| \tag{18}$$

In these equations, $\mathbf{cH}_{\mathrm{i}}$, $\mathbf{cV}_{\mathrm{i}}$, and $\mathbf{cD}_{\mathrm{i}}$ represent the matrices of wavelet detail coefficients in the horizontal, vertical, and diagonal directions, respectively, corresponding to the *i*th vibration mode. These matrices are obtained via two-dimensional wavelet analysis of a signal defined based on the initial and current shapes of mode i [56]. Furthermore, the coefficients $\mathrm{I}_{\mathrm{f}}^{\mathrm{H}}$, $\mathrm{I}_{\mathrm{f}}^{\mathrm{V}}$, and $\mathrm{I}_{\mathrm{f}}^{\mathrm{D}}$ are defined according to Eqs. (19) to (21) [56].

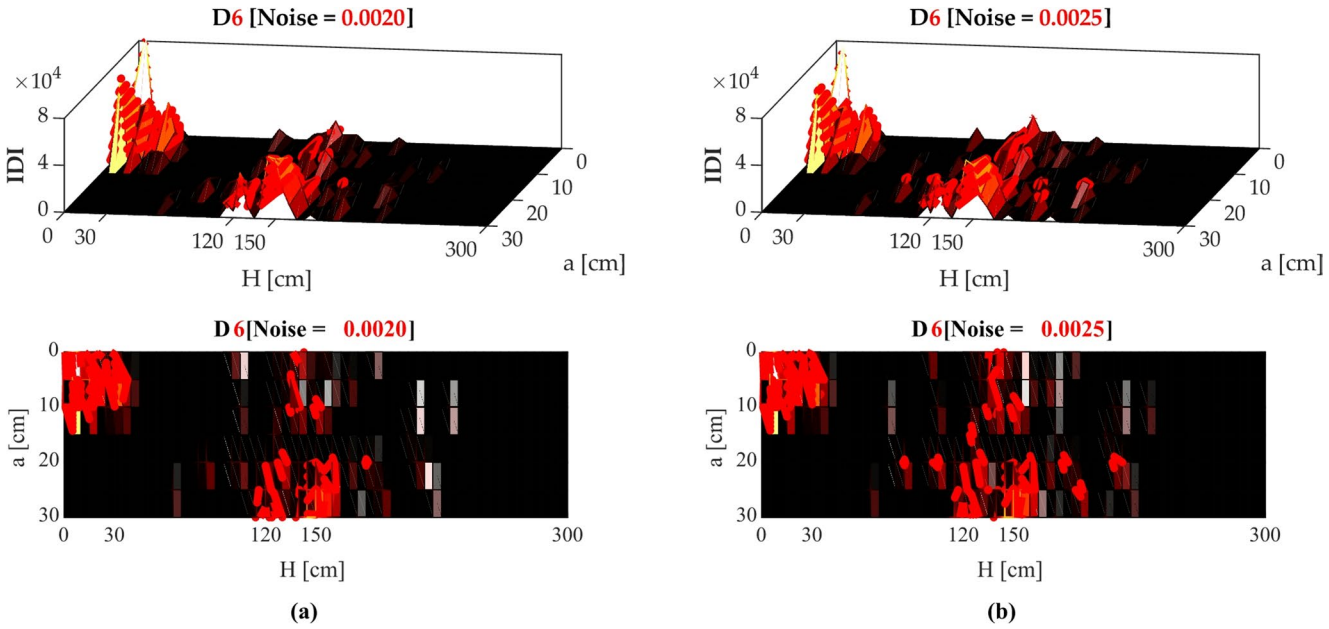


**Fig. 12** Surface plot of the **IDI** showing peaks of irregularities and disturbances for the damaged state D6 under noise levels: (**a**) 0.0020 and (**b**) 0.0025

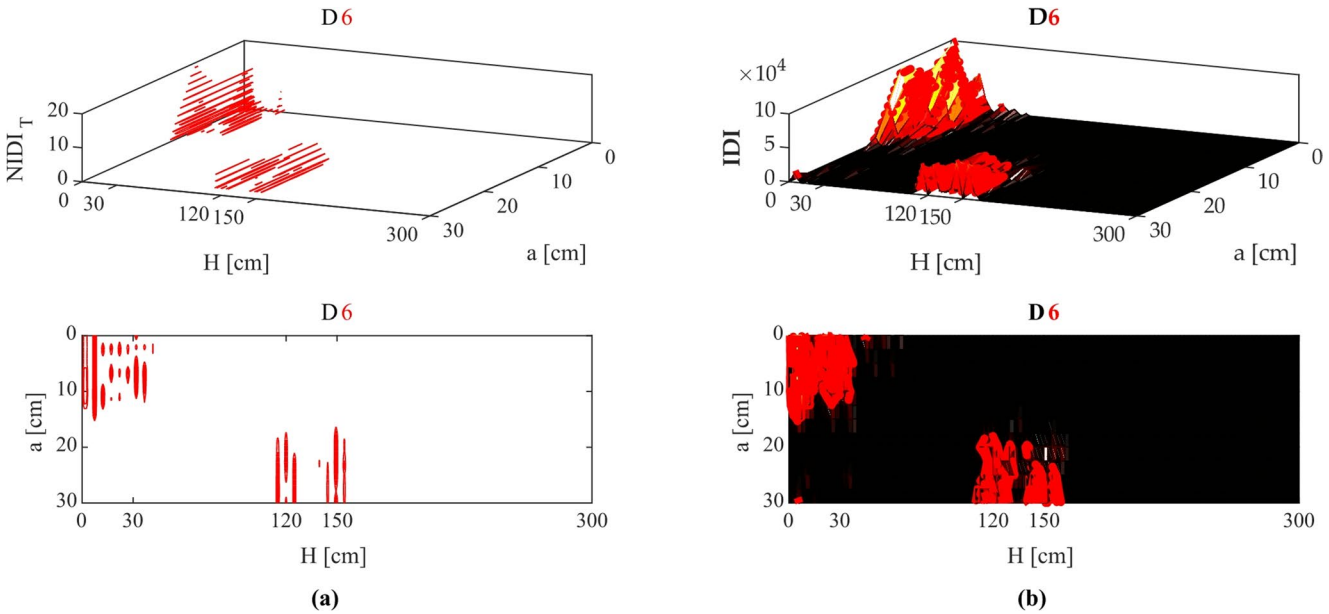


**Fig. 13** Comparative visualization of debonding detection results: (**a**) Wavelet feature extraction method [56]; (**b**) Proposed IDI method

$$I_f^H = I_f \frac{\max(|\mathbf{cH}_i(:)|)}{M} \tag{19}$$

$$I_f^V = I_f \frac{\max(|\mathbf{cV}_i(:)|)}{M} \tag{20}$$

$$I_f^D = I_f \frac{\max(|\mathbf{cD}_i(:)|)}{M} \tag{21}$$

In Eqs. (19) to (21), $\mathbf{I}_f$ is referred to as an effective identification factor, and its value is considered to range between 0 and 0.5. Additionally, M is defined according to Eq. (22) [56].

$$M = \max([\max(|\mathbf{cH}_i(:)|) \quad \max(|\mathbf{cV}_i(:)|) \quad \max(|\mathbf{cD}_i(:)|)]) \tag{22}$$

The method [56] was implemented using an $\mathbf{I}_f$ value of 0.25 and performing wavelet analysis with the "rbio5.5" wavelet function as an example for the D6 damage scenario, and the $NIDI_T$ was calculated. The damage detection results based on [56], as well as the proposed method of this study, are presented in Fig. 13. It can be observed that the proposed method of this study, compared to [56], was able to identify regions of concrete-steel debonding with a higher degree of accumulation and clustering of significant irregularities. It should be noted that although the IDI formulations proposed in this study are not as computationally complex as the $NIDI_T$ formulations, their diagnostic results are, nevertheless, more favorable compared to $NIDI_T$.

## Verification of IDI-Based Damage Localization Through Calibrated Modeling

The proposed method in this study demonstrates not only satisfactory performance in detecting debonding-type damage in CFST columns, but also proves effective in identifying various other types of damage in beam- and column-like structural elements. Microcracks and cracks are among the most common forms of structural damage. In CFST columns, the propagation and concentration of microcracks at the interface between the concrete core and the steel tube are key factors contributing to surface debonding between these two components. Although the primary focus of this research is on identifying surface debonding in CFST columns, this section specifically examines the detection of cracking in a cantilever beam (Fig. 14) selected from the study and experimental validation by Rucka and Wilde [69, 70], in order to demonstrate the broader applicability of IDI. This analysis not only confirms the diagnostic capabilities of IDI, but also illustrates that its utility extends beyond detecting debonding in CFST columns and can be generalized to other types of structural damage.

To assess and verify the diagnostic performance of the proposed method for damage detection and localization, the cantilever beam studied by Rucka and Wilde [69, 70] was modeled in finite element software. The beam's geometric dimensions are specified as L = 480 mm, B = 60 mm, H = 20 mm, $L_1$ = 120 mm, $L_r$ = 2 mm, and a = 7 mm. The material properties used in the simulation are defined as: Young's modulus E = 3420 MPa, Poisson's ratio ν = 0.30, and density ρ = 1187 kg/m$^3$.

Rucka and Wilde [69] recorded modal displacements at 48 locations along the beam to construct the first mode shape and reported the corresponding natural frequency as 23.375 Hz. In this study, finite element modeling of the beam was carried out using solid elements, based on the previously defined geometric parameters. Following the assignment of material properties, a frequency analysis was performed across multiple mesh densities. To validate the model's accuracy, the resulting mode shapes and natural frequencies from the simulation were compared with the experimental results provided by Rucka and Wilde. The results indicated that using an 8 mm mesh size for the modal analysis of the cracked beam yielded a natural frequency of 23.252 Hz. The discrepancy between the finite element results and the experimental data was calculated to be only 0.526%, confirming the high accuracy of the numerical model. Furthermore, the mode shape obtained from the finite element analysis is presented alongside the experimental mode shape in Fig. 15. The direction of nodal displacements, along with the curvature and concavity patterns, show strong agreement between the numerical and experimental results, with only negligible differences in nodal displacements.

The IDI was applied to detect and localize the crack within the cantilever beam. The IDI was calculated using the mode shapes presented in Fig. 16. Following the assignment of irregularity values to the nodes, a

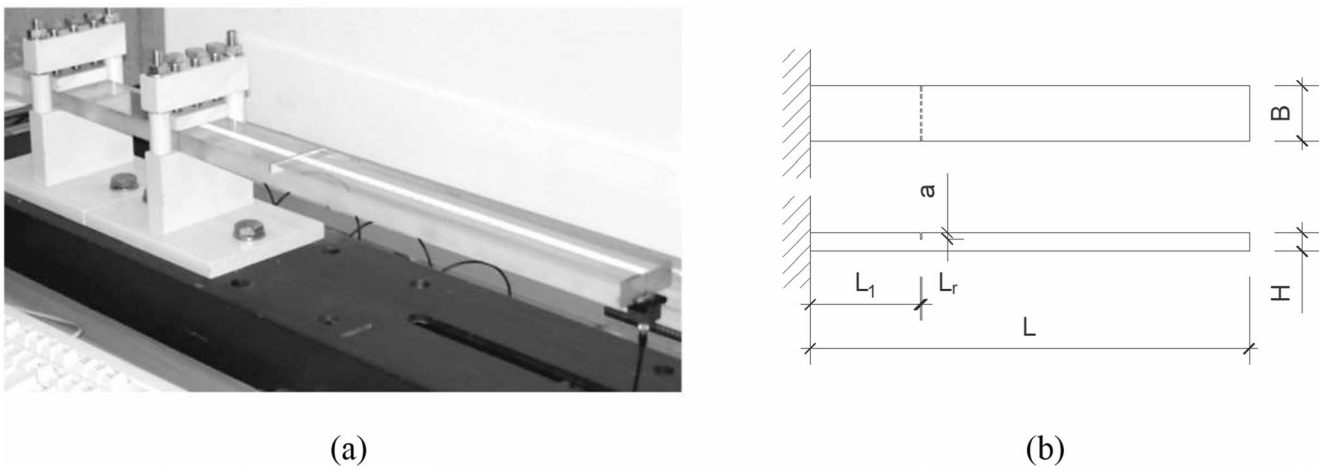


**Fig. 14** Cracked cantilever beam: (**a**) Experimental set-up [70], (**b**) Schematic of the cracked location [69, 70]

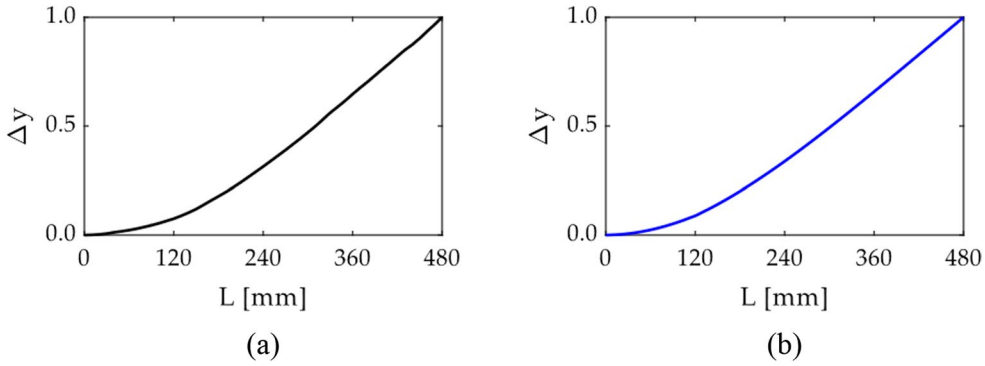


**Fig. 15** First mode shape of the cracked beam: (**a**) Experimental, (**b**) Numerical

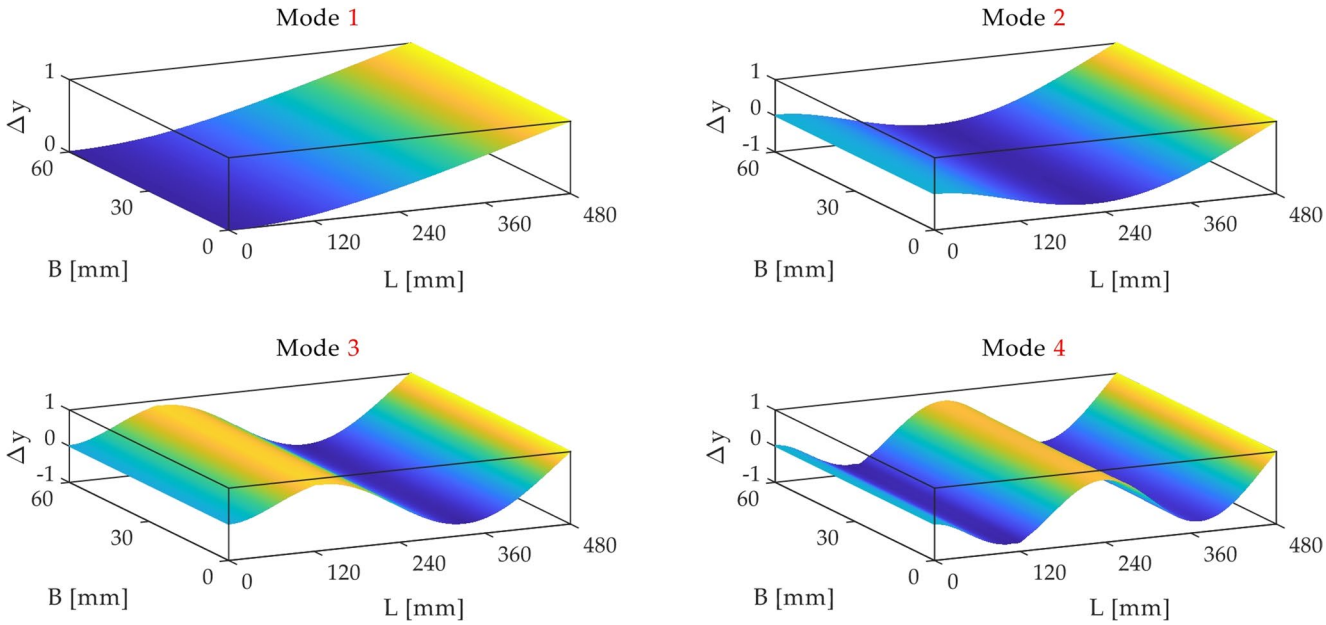


**Fig. 16** The first four vibration mode shapes of the cracked beam

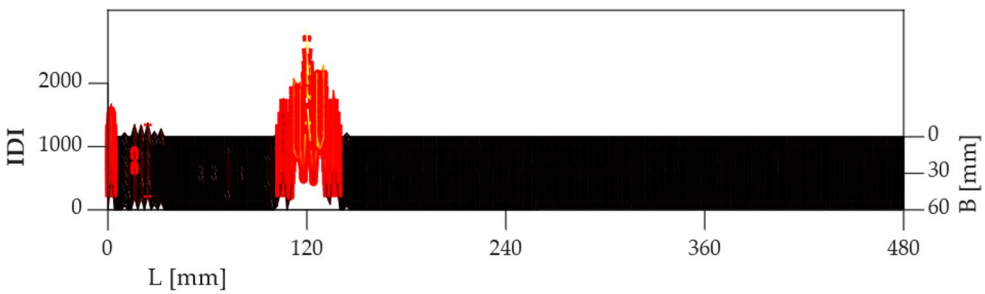


**Fig. 17** Surface plot of the **IDI** showing peaks of irregularities and disturbances for the cracked beam

concentration of elevated irregularity peaks was observed at the crack location (Fig. 17). These irregularities were significantly more pronounced in the vicinity of the crack compared to other regions of the beam. The results confirm that IDI demonstrates reliable performance and high accuracy in detecting differences between intact and damaged zones in beam-type structural elements.

## Conclusions

This study investigated the influence of interface debonding on the dynamic modal characteristics of CFST columns and introduced an original vibration-driven computational approach, termed the IDI, for identifying such defects. The key findings and implications are summarized below:

- Effect of Debonding on Dynamic Response
  Interface debonding, as one of the common types of damage in CFST columns, leads to reductions in natural frequencies and changes in mode shapes. The asymmetry observed in the **MAC** and **θ** matrices reflects variations between the initial and current modal shapes under damaged conditions. The diagonal elements of the **MAC** matrix are less than 1, and those of the **θ** matrix deviate from zero, indicating a lack of conformity between the corresponding mode shapes. In contrast, diagonal values of 1 (for **MAC**) and 0 (for **θ**), together with symmetric matrices, represent the undamaged state.
- Development and Application of the IDI
  By utilizing the initial and current shapes of vibration modes along with the concept of curvature, the proposed IDI demonstrated reliable numerical performance in identifying concrete–steel debonding regions. In the conducted analyses, the aggregation and clustering of irregularities occurred as pronounced peaks in the debonded areas, thereby allowing the damaged regions to be clearly distinguished from the intact zones. The actual debonding extents, as specified in Tables 2 and 10; Figs. 1 and 6, were captured in the **IDI** surface plots, and the comparison between the detected and actual debonding regions confirmed the diagnostic capability of the IDI. Notably, this approach effectively identified damaged areas near the boundary edges and at the column base—locations that are typically challenging for damage localization in SHM, particularly for signal-processing-based methods.
- Sensitivity to Random Noise
  Under laboratory-like conditions and at low levels of random noise (Section Numerical Evaluation of IDI Sensitivity To Random Noise), the IDI exhibited stable behavior, with diagnostic peaks corresponding to the actual debonding regions remaining clearly distinguishable. This demonstrates the promising stability and effectiveness of the method in damage identification.
- Comparison with a Novel Wavelet Feature Extraction Method
  Comparative analysis with a recently developed wavelet-based feature extraction technique [56] (Section Validation of IDI Diagnostic Performance Using a Novel Wavelet-Based Feature Extraction Method) indicated that the proposed IDI achieved superior localization performance while maintaining lower computational complexity.
- Verification on Beam-Type Elements
  The application of the IDI to a cracked cantilever beam demonstrated that the method can be extended beyond CFST columns to other beam-like structures, different damage types, and boundary conditions (Section Verification of IDI-Based Damage Localization Through Calibrated Modeling).
- Limitations and Future Work
  Although this study is based on finite element simulations, the findings provide a foundation for future experimental validation. Further research could focus on experimental verification, combining the IDI with noise-filtering techniques for applications under higher noise levels, or integrating it with other approaches to develop a multi-stage diagnostic framework, as well as testing the IDI under multiple damage scenarios and boundary conditions.

Overall, the numerical results demonstrated that the proposed IDI method provides a promising and computationally efficient framework for identifying interface debonding and other localized damages in structural elements, supporting its potential application in SHM.

**Acknowledgements** The authors would like to express gratitude and appreciation to Prof. M. Rucka for sharing the laboratory experimental data [69, 70] for the cracked cantilever beam.

**Author Contributions** Conceptualization, A.S.T., M.K., and D.-P.N.K.; Methodology, M.K., D.-P.N.K., and S.M.; Software, M.K., D.-P.N.K., and B.D.; Validation, A.S.T., M.K., D.-P.N.K., and S.M.; Formal Analysis, M.K. and D.-P.N.K.; Investigation, M.K., D.-P.N.K., and S.M.; Resources, M.K., D.-P.N.K., and B.D.; Data Curation, A.S.T., M.K., D.-P.N.K., and B.D.; Writing—Original Draft Preparation, M.K., D.-P.N.K., and S.M.; Writing—Review and Editing, A.S.T., M.K., and D.-P.N.K.; Visualization, A.S.T., M.K., D.-P.N.K., and B.D.; Supervision, D.-P.N.K. All authors have read and agreed to the published version of the manuscript.

**Funding** Open access funding provided by HEAL-Link Greece. This research received no external funding.

**Data Availability** The original contributions presented in this study are included in the article. Further inquiries can be directed to the corresponding author.

## Declarations

**Conflict of interest** The authors declare no conflict of interest.

## References


1. Benaddi H, Rebai B, Messas T, Salhi M (2024) Evaluation of self-compacting concrete for concrete repair applications. Res Eng Struct Mater 11:495–513. https://doi.org/10.17515/resm2024.255st0423rs
2. Rebai B, Tidjani M (2025) Buckling analysis of functionally graded plates: influence of homogenization, geometry, and porosity. J Press Vessel Technol 147:061304. https://doi.org/10.1115/1.4069156
3. Gharehbaghi VR, Noroozinejad Farsangi E, Noori M, Yang TY, Li S, Nguyen A, Málaga-Chuquitaype C, Gardoni P, Mirjalili S (2022) A critical review on structural health monitoring: definitions, methods, and perspectives. Arch Comput Methods Eng 29:2209–2235. https://doi.org/10.1007/s11831-021-09665-9
4. Gharehbaghi V, Noroozinejad Farsangi E, Yang TY, Noori M, Kontoni D-PN (2022) A novel computer-vision approach assisted by 2D-wavelet transform and locality sensitive discriminant analysis for concrete crack detection. Sensors 22:8986. https://doi.org/10.3390/s22228986
5. Hassani S, Dackermann U (2023) A systematic review of advanced sensor technologies for non-destructive testing and structural health monitoring. Sensors 23:2204. https://doi.org/10.3390/s23042204
6. Zhou Y, Ma Z, Fu L (2025) A review of key signal processing techniques for structural health monitoring: highlighting non-parametric time-frequency analysis, adaptive decomposition, and deconvolution. Algorithms. https://doi.org/10.3390/a18060318
7. Dahmani M, Arbaoui A, Rebai B (2025) Wavelet signal analysis for the detection of sand excess defects in hardened concrete. Res Eng Struct Mater. https://doi.org/10.17515/resm2025-735ma0309rs
8. Mansouri S (2021) The investigation of the effect of using energy dissipation equipment in seismic retrofitting an exist highway RC bridge subjected to far-fault earthquakes. Int J Bridg Eng 9:51–84
9. Mansouri S, Noroozinejad Farsangi E (2024) Adequacy of equivalent static analysis method employing Caltrans, AASHTO, and ATC-32 provisions in response estimation of vibration-controlled bridges. Pract Period Struct Des Constr. https://doi.org/10.1061/ppscfx.sceng-1340
10. Mardanshahi A, Sreekumar A, Yang X, Barman SK, Chronopoulos D (2025) Sensing techniques for structural health monitoring: a state-of-the-art review on performance criteria and new-generation technologies. Sensors 25:1424. https://doi.org/10.3390/s25051424
11. Dharmajan NB, AlHamaydeh M (2025) State-of-the-art review of structural vibration control: overview and research gaps. Appl Sci. https://doi.org/10.3390/app15147966
12. Pandey AK, Biswas M, Samman MM (1991) Damage detection from changes in curvature mode shapes. J Sound Vib 145:321–332. https://doi.org/10.1016/0022-460X(91)90595-B
13. Yam LH, Li YY, Wong WO (2002) Sensitivity studies of parameters for damage detection of plate-like structures using static and dynamic approaches. Eng Struct 24:1465–1475. https://doi.org/10.1016/S0141-0296(02)00094-9
14. Sahoo B, Maity D (2007) Damage assessment of structures using hybrid neuro-genetic algorithm. Appl Soft Comput 7:89–104. https://doi.org/10.1016/j.asoc.2005.04.001
15. Shih HW, Thambiratnam DP, Chan THT (2009) Vibration based structural damage detection in flexural members using multi-criteria approach. J Sound Vib 323:645–661. https://doi.org/10.1016/j.jsv.2009.01.019
16. Roveri N, Carcaterra A (2012) Damage detection in structures under traveling loads by Hilbert-Huang transform. Mech Syst Signal Process 28:128–144. https://doi.org/10.1016/j.ymssp.2011.06.018
17. Bao C, Hao H, Li ZX (2013) Multi-stage identification scheme for detecting damage in structures under ambient excitations. Smart Mater Struct. https://doi.org/10.1088/0964-1726/22/4/045006
18. Xu X, Zhang F, Zhu W (2013) Damage detection of continuous box girder based on modal flexibility curvature method. Adv Mater Res 671–674:1016–1020. https://doi.org/10.4028/www.scientific.net/AMR.671-674.1016
19. Sun D, Ren Q (2016) Seismic damage analysis of concrete gravity dam based on wavelet transform. Shock Vib. https://doi.org/10.1155/2016/6841836
20. Nobahari M, Ghasemi MR, Shabakhty N (2017) A novel heuristic search algorithm for optimization with application to structural damage identification. Smart Struct Syst 19:449–461. https://doi.org/10.12989/sss.2017.19.4.449
21. Abbasnia R, Mirzaei B, Yousefbeik S (2016) A two-step method composed of wavelet transform and model updating method for multiple damage diagnosis in beams. J Vibroeng 18:1497–1513. https://doi.org/10.21595/jve.2016.16721
22. Mirzaei B, Nasrollahi K, Yousefbeik S, Amiri GG, Hosseinzadeh AZ (2019) A two-step method for damage identification and quantification in large trusses via wavelet transform and optimization algorithm. J Rehabil Civ Eng 7:1–20. https://doi.org/10.22075/jrce.2017.11678.1197
23. Yang ZB, Radzienski M, Kudela P, Ostachowicz W (2017) Fourier spectral-based modal curvature analysis and its application to damage detection in beams. Mech Syst Signal Process 84:763–781. https://doi.org/10.1016/j.ymssp.2016.07.005
24. Yang C, Oyadiji SO (2017) Delamination detection in composite laminate plates using 2D wavelet analysis of modal frequency surface. Comput Struct 179:109–126. https://doi.org/10.1016/j.compstruc.2016.10.019
25. Kourehli SS (2017) Application of extreme learning machine to damage detection of plate-like structures. Int J Struct Stab Dyn. https://doi.org/10.1142/S0219455417500687
26. Darvishan E (2019) Damage detection of cable-stayed bridges using frequency domain analysis and clustering. Amirkabir J Civ Eng 51:767–780. https://doi.org/10.22060/ceej.2018.14141.5568
27. Hanteh M, Rezaifar O (2021) Damage detection in precast full panel building by continuous wavelet analysis analytical method. Structures 29:701–713. https://doi.org/10.1016/j.istruc.2020.12.002
28. Hanteh M, Rezaifar O, Gholhaki M (2021) Selecting the appropriate wavelet function in the damage detection of precast full panel building based on experimental results and wavelet analysis. J Civ Struct Heal Monit 11:1013–1036. https://doi.org/10.1007/s13349-021-00497-6
29. Bakhshi A, Mousavi M (2022) Crack detection in masonry structures using computer vision based on deep learning. Sharif J Civ Eng 38(2):99–108. https://doi.org/10.24200/j30.2022.59496.3055
30. Mousavi M, Bakhshi A (2022) Crack detection in concrete members using encoder-decoder models based on deep learning. Sharif J Civ Eng 382:79–88. https://doi.org/10.24200/j30.2022.59482.3054
31. Ghannadi P, Kourehli SS (2022) Efficiency of the slime mold algorithm for damage detection of large-scale structures. Struct Des Tall Spec Build. https://doi.org/10.1002/tal.1967
32. Silik A, Noori M, Ghiasi R, Wang T, Kuok SC, Farhan NSD, Dang J, Wu Z, Altabey WA (2023) Dynamic wavelet neural network model for damage features extraction and patterns recognition. J Civ Struct Heal Monit 13:925–945. https://doi.org/10.1007/s13349-023-00683-8
33. Chen D, Zhang Y, Xu S, Li Z, Yang C (2023) Experimental study on bridge structural damage identification based on quasi-static displacement effects and wavelet packet decomposition. Buildings 13:2974. https://doi.org/10.3390/buildings13122974
34. Kordestani H, Zhang C, Arab A (2023) An output-only, energy-based, damage detection method using the trend lines of the structural acceleration response. Buildings 13:3007. https://doi.org/10.3390/buildings13123007
35. Zhou Y, Zhuang Y, Sinha JK (2024) Damage identification in steel girder based on vibration responses of different sinusoidal

excitations and wavelet packet permutation entropy. Appl Sci 14:7871. https://doi.org/10.3390/app14177871
36. Khanahmadi M (2024) An effective vibration-based feature extraction method for single and multiple damage localization in thin-walled plates using one-dimensional wavelet transform: a numerical and experimental study. Thin-Walled Struct 204:112288. https://doi.org/10.1016/j.tws.2024.112288
37. Khanahmadi M, Mirzaei B, Amiri GG, Gholhaki M, Rezaifar O (2024) Vibration-based damage localization in 3D sandwich panels using an irregularity detection index (IDI) based on signal processing. Measurement 224:113902. https://doi.org/10.1016/j.measurement.2023.113902
38. Soleimani Nezhad S, Khademian F, Naderpour H, Kalantari SM, Fakharian P (2024) Signal processing-based damage detection of steel braced frame subjected to consequent excitations. Innov Infrastruct Solut. https://doi.org/10.1007/s41062-024-01762-5
39. Hassani S, Dackermann U, Mousavi M, Li J (2024) A systematic review of data fusion techniques for optimized structural health monitoring. Inf Fusion. https://doi.org/10.1016/j.inffus.2023.102136
40. Hassani S, Dackermann U, Mousavi M, Li J (2024) Enhanced damage detection for noisy input signals using improved reptile search algorithm and data analytics techniques. Computers & Structures. https://doi.org/10.1016/j.compstruc.2024.107293
41. Ghannadi P, Kourehli SS, Nguyen A (2024) Experimental validation of an efficient strategy for FE model updating and damage identification in tubular structures. Nondestruct Test Eval 1–40. https://doi.org/10.1080/10589759.2024.2402887
42. Rodriguez S, Rébillat M, Paunikar S, Margerit P, Monteiro E, Chinesta F, Mechbal N (2025) Single atom convolutional matching pursuit: theoretical framework and application to Lamb waves based structural health monitoring. Signal Process. https://doi.org/10.1016/j.sigpro.2025.109898
43. Xu B, Li B, Song G (2013) Active debonding detection for large rectangular CFSTs based on wavelet packet energy spectrum with piezoceramics. J Struct Eng 139:1435–1443. https://doi.org/10.1061/(asce)st.1943-541x.0000632
44. Xu B, Zhang T, Song G, Gu H (2013) Active interface debonding detection of a concrete-filled steel tube with piezoelectric technologies using wavelet packet analysis. Mech Syst Signal Process 36:7–17. https://doi.org/10.1016/j.ymssp.2011.07.029
45. Xu B, Chen H, Mo YL, Zhou T (2018) Dominance of debonding defect of CFST on PZT sensor response considering the meso-scale structure of concrete with multi-scale simulation. Mech Syst Signal Process 107:515–528. https://doi.org/10.1016/j.ymssp.2018.01.041
46. Xu B, Chen H, Xia S (2017) Wave propagation simulation and its wavelet package analysis for debonding detection of circular CFST members. Smart Struct Syst 19:181–194. https://doi.org/10.12989/sss.2017.19.2.181
47. Xu B, Chen H, Xia S (2017) Numerical study on the mechanism of active interfacial debonding detection for rectangular CFSTs based on wavelet packet analysis with piezoceramics. Mech Syst Signal Process 86:108–121. https://doi.org/10.1016/j.ymssp.2016.10.002
48. Xu B, Chen H, Mo YL, Chen X (2017) Multi-physical field guided wave simulation for circular concrete-filled steel tubes coupled with piezoelectric patches considering debonding defects. Int J Solids Struct 122:25–32. https://doi.org/10.1016/j.ijsolstr.2017.05.040
49. Younesi A, Rezaifar O, Gholhaki M, Esfandiari A (2019) Structural health monitoring of a concrete-filled tube column. Mag Civ Eng 85:136–145. https://doi.org/10.18720/MCE.85.11
50. Younesi A, Rezaifar O, Gholhaki M, Esfandiari A (2021) Active interface debonding detection of a concrete filled tube (CFT) column by modal parameters and continuous wavelet transform (CWT) technique. Struct Monit Maint 8:69–90. https://doi.org/10.12989/smm.2021.8.1.069
51. Chen H, Xu B, Wang J, Luan L, Zhou T, Nie X, Mo Y-L (2019) Interfacial debonding detection for rectangular CFST using the MASW method and its physical mechanism analysis at the meso-level. Sensors 19:2778. https://doi.org/10.3390/s19122778
52. Chen H, Xu B, Zhou T, Mo Y-L (2019) Debonding detection for rectangular CFST using surface wave measurement: test and multi-physical fields numerical simulation. Mech Syst Signal Process 117:238–254. https://doi.org/10.1016/j.ymssp.2018.07.047
53. Mamazizi A, Khanahmadi M, Nobakht Vakili K (2022) Debonding damage detection and assessment in a CFST composite column using modal dynamic data. Sharif J Civ Eng 38(2):53–63. https://doi.org/10.24200/J30.2022.59903.3075
54. Liu H, Chen Z, Liu Y, Chen Y, Du Y, Zhou F (2023) Interfacial debonding detection for CFST structures using an ultrasonic phased array: application to the Shenzhen SEG building. Mech Syst Signal Process. https://doi.org/10.1016/j.ymssp.2023.110214
55. Gholhaki M, Mirzaei B, Khanahmadi M, Amiri GG, Rezaifar O (2024) A numerical study on vibration-based interface debonding detection of CFST columns using an effective wavelet-based feature extraction technique. Steel Compos Struct 53:45–59. https://doi.org/10.12989/scs.2024.53.1.045
56. Khanahmadi M, Mirzaei B, Amiri GG, Gholhaki M, Rezaifar O (2025) A mode shape sensitivity-based wavelet feature extraction method for interface debonding detection in concrete-filled steel tubes. Meas Sci Technol 36:016137. https://doi.org/10.1088/1361-6501/ad8adf
57. Wang C, Yang Y, Fan G, Lian J, Chen F (2024) Detection of debonding defects in concrete-filled steel tubes using fluctuation analysis method. Sensors 24:8222. https://doi.org/10.3390/s24248222
58. Khanahmadi M, Khalighi M (2024) Interfacial debonding detection in concrete-filled steel tubular (CFST) columns with modal curvature-based irregularity detection indices. Int J Struct Stab Dyn 24:2450148. https://doi.org/10.1142/s0219455424501487
59. Cao H, Li J, Chen X (2025) Investigation of interfacial debonding identification for concrete filled steel tube columns based on acoustic signals. Measurement 240:115511. https://doi.org/10.1016/j.measurement.2024.115511
60. Yao M, Chen Z, Li J, Guan S, Tang Y (2025) Ultrasonic identification of CFST debonding via a novel Bayesian Optimized-LSTM network. Mech Syst Signal Process. https://doi.org/10.1016/j.ymssp.2025.113175
61. Mirzaei B, Khanahmadi M, Rezaifar O, Gholhaki M, Amiri GG (2025) Efficient modal flexibility signal processing methodology for innovative identification of debonding zones in concrete-filled steel tubes. Results Eng 26:104683. https://doi.org/10.1016/j.rineng.2025.104683
62. ANSI/AISC 360–16 (2016) Specification for structural steel buildings. Am Inst Steel Constr. 1–612
63. Khanahmadi M, Gholhaki M, Rezaifar O, Dezhkam B (2023) Signal processing methodology for detection and localization of damages in columns under the effect of axial load. Measurement 211:112595. https://doi.org/10.1016/j.measurement.2023.112595
64. Naderpour H, Fakharian P (2016) A synthesis of peak picking method and wavelet packet transform for structural modal identification. KSCE J Civ Eng 20:2859–2867. https://doi.org/10.1007/s12205-016-0523-4

65. Rezaifar O, Kabir MZ, Taribakhsh M, Tehranian A (2008) Dynamic behaviour of 3D-panel single-storey system using shaking table testing. Eng Struct 30:318–337. https://doi.org/10.1016/j.engstruct.2007.03.019
66. Ghannadi P, Kourehli SS (2019) Structural damage detection based on MAC flexibility and frequency using moth-flame algorithm. Struct Eng Mech 70:649–659. https://doi.org/10.12989/sem.2019.70.6.649
67. Khanahmadi M, Mirzaei B, Dezhkam B, Rezaifar O, Gholhaki M, Amiri GG (2024) Vibration-based health monitoring and damage detection in beam-like structures with innovative approaches based on signal processing: a numerical and experimental study. Structures 68:107211. https://doi.org/10.1016/j.istruc.2024.107211
68. Khanahmadi M (2025) A cutting-edge framework for damage-sensitive feature extraction leveraging modal dynamic flexibility in signal processing-driven structural health monitoring. Thin-Walled Struct. https://doi.org/10.1016/j.tws.2025.113617
69. Rucka M, Wilde K (2006) Application of continuous wavelet transform in vibration based damage detection method for beams and plates. J Sound Vib 297:536–550. https://doi.org/10.1016/j.jsv.2006.04.015
70. Rucka M, Wilde K (2010) Neuro-wavelet damage detection technique in beam, plate and shell structures with experimental validation. J Theor Appl Mech 48:579–604